Hyperspectral Imaging Small Satellite in Multi-Agent Marine Observation System

Mariusz E. Grøtte[1], Roger Birkeland[2], João F. Fortuna[1,3], Julian Veisdal[2,4], Milica Orlandic[2], Evelyn Honoré-Livermore[2], Gara Quintana-Díaz[2], Harald Martens[1,3], J. Tommy Gravdahl[1], Fred Sigernes[4], Jan Otto Reberg[3], Geir Johnsen[3,5], Kanna Rajan[1,6], Tor A. Johansen[1]

***Abstract*— HYPer-spectral Smallsat for ocean Observation (`HYPSO`), which is of a standard CubeSat design, will observe ocean color in the coast of Norway, specifically targeted to detect algal blooms, phytoplankton, river plumes etc. The payload, a push-broom type hyperspectral imager (HSI), will image a 50×70 km^2 target area. `HYPSO` will perform a slew maneuver to attain sufficient overlapping exposures to increase effective spatial resolution and signal-to-noise ratio. Following are the operational phases: a) uplink of mission planning and task execution data from nearby ground station prior to observing the target; b) preparations for slew maneuver; c) imaging operations; d) data processing where geometric, spectral and spatio-temporal processing of the hyperspectral cube will happen onboard; and finally e) downlink of data to a nearby ground station. `HYPSO` will be in a Sun-Synchronous Orbit in order to ensure best illumination conditions of target. Mission design, simulations and analysis have verified the concept to be feasible with respect to operations, data handling and imaging performance with limiting factors being spacecraft size, power consumption as well as cloud cover and short time of peak-season during summer in Norway. `HYPSO` is planned to be launched in Q4 2019 and will directly augment and constitute a coordinated robotic platform consisting of UAVs, ASVs and AUVs for synoptic ocean observations. After successful first-flight, a second mission is planned to be launched in Q4 2020 and then followed by a pipeline of nanosatellites with different technological solutions to be developed for diverse missions related to oceanography.**

I. Introduction

As a sink for green-house gases and as the environment of marine life and resources, the oceans' role and evolving state, is undeniable. Within this context of the changing global oceans, scientists, technologists, policy makers and the general public have come to understand the importance of the world's ocean on our well-being and to those who will inhabit the planet in the future – near and distant. The influence of the changing climate and its impact on the 70% of the planet covered by water, needs to be studied at resolutions from the fine scale (for micro-biology) to the large (large atmospheric phenomenon such as hurricanes, the extent of the global ice melt, harmful algal blooms, fronts). Traditional methods of making measurements in the ocean are not sustainable and/or are inflexible; ship-based measurements require extensive engineering and science infrastructure and support in addition to subjecting people to the harsh seafaring conditions. They also typically lead to point measurements for phenomenon spread over large spatial extents. Expensive multi-national remote sensing capabilities which require consensus driven management, not to mention years

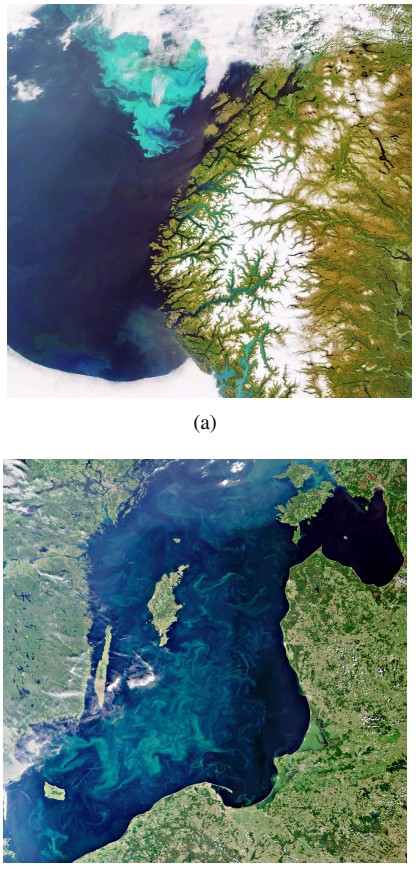

(a)

(b)

Fig. 1. Phytoplankton blooms observed from space. 1(a) Bloom observed 10th June 2006 by Envisat's MERIS instrument off the coast of Norway and 1(b) observed in the Baltic Sea acquired by MERIS on 11th July 2010. *Image courtesy: ESA*

[1]Center for Autonomous Marine Operations and Systems (AMOS), Department of Engineering Cybernetics, Norwegian University of Science and Technology, Trondheim, Norway.

[2]Department of Electronic Systems, Norwegian University of Science and Technology, Trondheim, Norway.

[3]IDLETechs AS, Trondheim, Norway.

[4]MOON Wearables, Trondheim, Norway.

[4]University Center Svalbard, Longyearbyen, Norway.

[5] Department of Biology, Norwegian University of Science and Technology, Trondheim, Norway.

[6]Faculty of Engineering, University of Porto, Portugal.

Corresponding author: tor.arne.johansen@itk.ntnu.no

of development and substantial ground support, to manage the inherent risks involved in building, flying and operating complex spacecraft costing in the millions of dollars. Both space and ocean offer hostile environments for exploration, yet provide critical clues to our origins and continuing well-being [1].

As an alternative approach, a network of autonomous underwater vehicles (AUVs), autonomous surface vehicles (ASVs) and unmanned aerial vehicles (UAVs) is capable of coordinated missions executed in concert with conventional vehicles, buoys and fixed sensor networks as envisioned in Autonomous Ocean Sampling Network (AOSN) [2], [3]. Such systems enable not only significant reduction in costs, and increased safety, but even more importantly provide substantially more and continuous information about the observed targets and features of scientific interest and do so *synoptically*. They do so by taking advantage of the complementary and coordinated capabilities of such autonomous assets related to position, range, endurance, mobility, sensors, and across large spatio-temporal scales for observing oceanographic phenomenon.

A variety of phenomenon of oceanographic interest can be detected from space. Sensors to detect are either optics or radar based. Our work is currently focused towards the former, typically in the context of looking at processes with large spatio-temporal extent, like algal blooms which have clear surface signatures (Figure I). Some blooms generate neurotoxins with significant impact to coastal marine and human populations [4].

A primary light-absorbing substance in the oceans is chlorophyll, which is involved in phytoplankton photosynthesis [5]. Plankton absorb the red and blue components of the light spectrum and reflect primarily green light. In addition, other substances that may be found dissolved in the water-column that can absorb light which are composed of organic carbon, often referred to as colored dissolved organic matter. A push-broom hyperspectral imager (HSI) operating in the visible and near-infrared (VNIR) spectrum can sweep over the ocean surface and capture 1-D line images with up to hundreds of narrow bands (less than 5 nm spectral resolution) in order to observe both organisms and matter in the upper water-column. From this information, the objective is to detect and characterize spatial extant extent of algal blooms [6], measure primary productivity using emittance from fluorescence generating micro-organisms, and other substances resulting from aquatic habitats and pollution to support environmental monitoring, climate research and marine resource management.

Using a proposed HSI payload integrated onto a small satellite platform (`SmallSat`) in space, in concert with aerial, surface, underwater vehicles, we propose an autonomous multi-agent system for marine observations. Figure 2 shows an operational view of such a system. There are several motivations for the need for such a combined and complementary capability, being:

- Traditional multi-purpose Earth observation (EO) satellites operated by agencies such as NASA and ESA provide excellent data covering the whole Earth. They may have medium to high spatial resolution, but usually have low temporal resolution since revisit times can be days to weeks and also low to medium spectral resolution (generally multispectral rather than hyperspectral), [7]. Our need is to augment upper water-column process studies where observing large tracts of the ocean and often to track changes over space and time requires a finer grained revisit time; typically this would be in the order of hours to a day.
- Dedicated (single-purpose) small satellites (nano- and micro-satellites, [8]) are operated to provide high spatial resolution by pointing an HSI with small field of view (FOV) to smaller (but still relatively large) target areas of interest, with shorter revisit times and potentially high spectral resolution. They may be using onboard remote sensor data analysis in order to detect features of special interest while obeying communication bandwidth constraints.
- Simultaneously, co-temporal observations from one or more UAVs with an HSI payload and ground-truth provided by in-situ platforms near the ocean surface can then be used to accurately measure and validate the features of interest at a much finer scale in the upper water column, and without the distortion from the atmosphere or being limited by cloud cover, cf. Figure 2.
- Finally, we hope to leverage the excitement of space flight, as a means to engage young researchers towards ocean monitoring, marine robotics and the systematic design and build of complex systems with the need to leverage advances in Artificial Intelligence and Robotics.

The components of such an autonomous multi-agent *cyber-physical system* must be tightly knit together by communication technology in combination with intelligent information processing and coordinated control as well as mission planning where tasks are dynamically allocated amongst the available assets and systems. Coordination in such a context

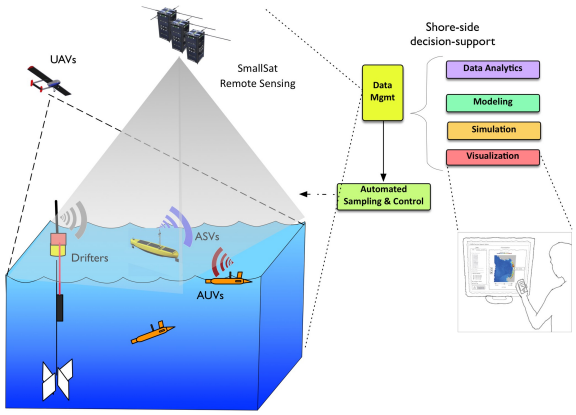

Fig. 2. Illustration of the main components in a multi-agent marine observation system.

would involve observing the same patch of the ocean co-temporally across diverse assets with a range of sensing techniques to piece together a comprehensive and cogent view.

While the use of an HSI for earth observation is not new (see [9], [8]), our focus exclusively as a tool for both oceanographic measurements and for synoptic in-situ field measurements is a novel approach with a significant potential for reducing cost and improving data quality in oceanography. Further, with the potential of targeting control, opportunistic events leading to event-response capabilities can be finely tailored to specific events and limited impacts to the public, e.g. Harmful Algal Blooms (HABs).

The main contribution of this work is on the mission design and concept of operations of a `SmallSat` with a small push-broom HSI called HYPer-spectral Smallsat for ocean Observation (`HYPSO`) which is part of an autonomous multi-agent observation system. `HYPSO` payload and S/C bus are under development and several versions of the `SmallSat` and multi-agent system are expected to be operational during the next years. In principle, `HYPSO` will be of a standardized CubeSat design.

This note is organized as follows:

1) Overview
2) Mission Design
3) Payload
4) Data Processing & Control
5) Attitude Determination & Control
6) Communications
7) Software-Defined Radio
8) Spacecraft Bus
9) Mission Analysis
10) Systems Engineering Methodology
11) Conclusions & Future Work
12) Acknowledgments
13) References

II. Overview

Figure 3 summarizes the capabilities of the different agents in an autonomous marine observation system, such as the one illustrated in Figure 2, dedicated for our intended application to ocean color observations with the HSI.

The right end of the horizontal spatial scale axis defines the spatial coverage of the HSI sensor system (defined as $\sqrt{(range \times swath)}$), while the left end defines the smallest spatial scales that can be captured by a HSI sensor on the platform. The upper end of the temporal capability defines the endurance of the platform, while the lower end illustrates the revisit time or fastest temporal scales that can be observed. It should be noted that the endurance of UAVs, USVs and AUVs may typically be easily extended by fast re-launch after re-fueling. We also remark that there are other important dimensions beyond the temporal and horizontal spatial scales that also characterize the differences between platforms. One important dimension is related to the maximum speed of UAVs, USVs and AUVs implying that

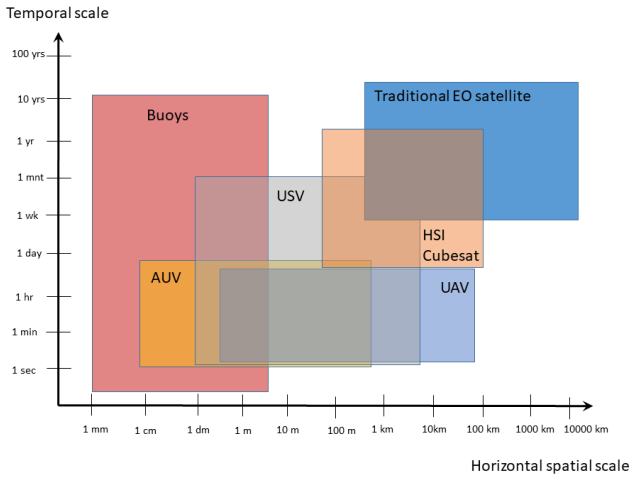

Fig. 3. Mapping of capabilities of various sensor platforms used for ocean color.

high temporal and spatial resolution can only be achieved within limited parts of areas that are within their range.

This means that these type of vehicles will need adaptive sampling and be guided towards "interesting" parts of the target area where it can be expected to make informative observations, [2]. Other important dimensions are related to weather sensitivities, payload weight limitations, and operational complexity. The figure clearly illustrates the complementary capabilities of the different sensor platforms, and shows the scope for a coordinated observation system that exploits the advantages of each platform type.

Based on Figure 3, `SmallSat` capability is generally differentiated from exquisite and monolithic optical EO satellites by having a better temporal, spectral and spatial resolution, but within a much smaller area and shorter lifetime. It is clear that a constellation with multiple HSI `SmallSat` will extend the capability in all dimensions compared to a single `SmallSat`. We also observe that a HSI `SmallSat` is a useful and complementary platform to AUVs, USVs, UAVs and buoys/drifters in particular given the limited mobility and speed of the mentioned platforms. In particular, the capabilities covered by `SmallSat`, UAV and USV are very well aligned by with requirements for observing highly transient phytoplankton blooms [10].

In order to achieve high spectral, spatial and temporal resolution of a HSI in a `SmallSat` system with low cost and low weight, our `HYPSO` design assumes that the observation target area is limited to a small number of patches of the Earth (possibly only one), typically at least of size 30 km$\times$30 km, cf. Figure 3. We emphasize that our system objective is not to map the entire Earth, but a tiny fraction corresponding to our specific target area(s) of interest. This enables the use of an imaging system with a relatively narrow FoV corresponding to a swath width of 70 km. By accurate attitude control and slewing motion, the push-broom HSI will sweep over this small area as illustrated in Figure 4.

TABLE I

HYPSO MISSION OVERVIEW

General	**Definition**
Objective	Ocean color
Subject	Coast of Norway
Target Location (baseline)	Lat: 63.867608 °, Lon: 8.663644 ° (Frøya, Norway)
Target area (in-track × cross-track)	50 km × 70 km
Orbit	
Type	10:00 AM/10:00 PM LTAN SSO
Altitude	500 km
Revisits to target	3
Launch	Q4 2019
Launch (successor)	Q3 2020
Payload	
Type	Pushbroom Hyperspectral Imager
Spectral Range	400-800 nm
Spectral Resolution	5-10 nm
Operating Modes	High Res; Medium Res
Instantaneous optical resolution	250 m (Nadir)
Swath Width	70.32 km
Ground Sampling Distance	39 m
Raw SNR per frame @ 500 nm	≈ 306 (1 mg/m^3 Chl-a)
S/C Bus	
Size	6U
Energy	54 Wh
Mass	≈7 kg
Autonomy	
Data Processing	Onboard geometric, radiometric, spectral and spatial processing
Downlinked Data Products	Level 2 and 4 (Levels 0, 1a, 1b and 3 upon request)
Operations	Uplink and downlink to Ground Station, tasks determined by mission control
Communications	
Bands	S-band (downlink); UHF (uplink)
Ground Stations	NTNU (Trondheim), Longyearbyen (Svalbard)

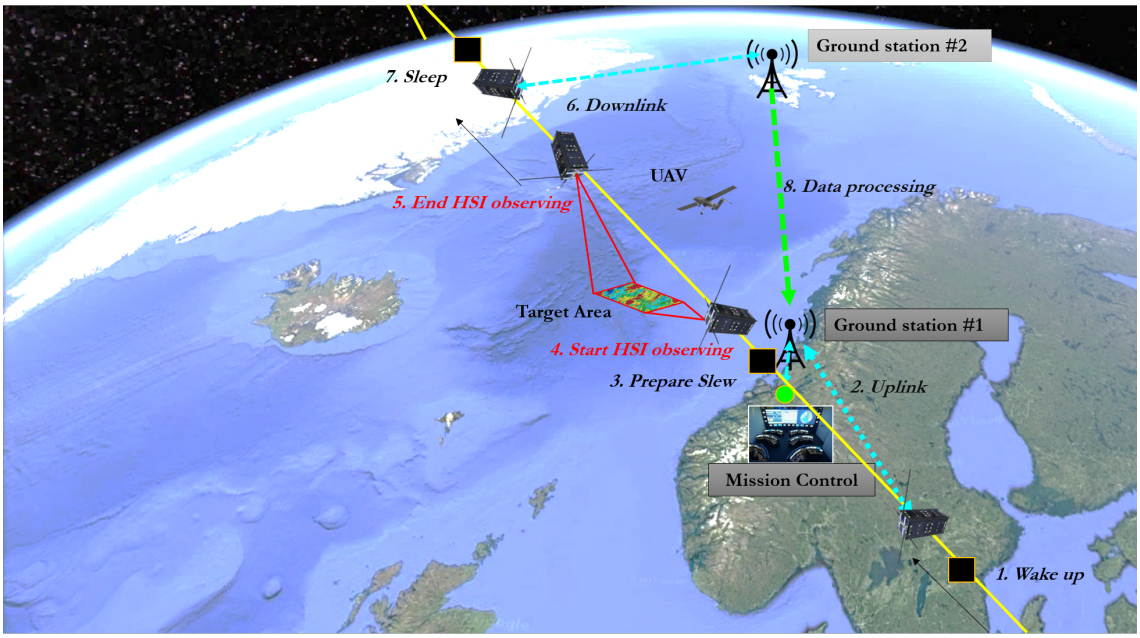

Fig. 4. Concept of operations for HYPSOin retrograde near-polar orbit.

The different phases in the operation of the HYPSO (as shown overall in Fig. 4) are characterized as follows:

1) Idle: HYPSO will spend most of its time in idle mode, where upon illumination it is harvesting solar energy.
2) Upload: HYPSO is scheduled to initialize operations in due time before it passes the target area. In preparation for the observation phase, if available, a nearby ground control station (GCS) uploads tasks and updates to the mission planning & scheduling of HYPSO . This may be changes in target area size and location, atmospheric variables, solar zenith angle, viewing zenith angle, ground sampling distance, cloud coverage observations and forecasts, camera gain setting and tuning, and data results from observations made by other assets (UAVs, USVs, etc.) to be used for calibration, or spectral and spatial signatures and other information on which target features to search for and report back on. [1]
3) Preparations: HYPSO activates mission-specific attitude control in order to be ready, pointing the sensing axis towards the target at a specific viewing zenith angle before actuation for spacecraft to move in opposite direction once it is aligned for imaging with settling time less than 1 min.
4) Start observation: HYPSO starts recording line scans from the HSI, while under slewing motion to scan slowly over the target area in order to maximize the spatial resolution along surface track by achieving GSD less than the payload's spatial resolution. With near-real-time geo-referenced data input, the images are fused in deconvolution filter or super-resolution/image fusion techniques. HYPSO stores the consecutive data which later undergo data analysis and compression algorithms onboard. Figure 4 illustrates the pushbroom HSI sweeping the target area, showing the need for attitude control and slewing motion. It also illustrates the complementary data captured by a for example UAV at the target area.
5) End observation and data processing: After the target area is scanned, HYPSO starts geometric, radiometric, spectral and spatio-temporal processing and automated analysis of the data cube in search of positive signatures that match a-priori reference data or unexpected signatures that are new to the model.
6) Download and idle: Depending on the location of the next GCS, HYPSO might directly downlink the results of its tasks, or go to idle-mode before scheduled to wake up again and initialize for communications at a later stage.
7) Other: imaging operations that are off-baseline image acquisitions of other target areas, i.e. larger targets and image size(s), other target locations, other data products, ground-space calibration, and on-orbit calibration.

[1]For example, a USV or UAV might tactically emit gas to form an artificial cloud of the size of at least one pixel at a suitable location and time such that it can be used to calibrate the satellite's HSI in space, time and spectrum.

III. Mission Design

Since the mission is highly oriented towards science and remote sensing, as well as being a technology demonstrator, it is necessary to establish *what* is needed and *how* the mission will be conducted operationally to achieve success. This is performed in the standard NASA/ESA framework for aerospace engineering projects. Mission design, or Pre-phase A and Phase A, motivate the particular use of HSI for ocean color purposes, and establishes how the SmallSat shall operate. Mission objectives, success criteria, requirements and constraints are established in Pre-phase A followed by analysis and characterization analysis for orbit, payload and operations in Phase A. Latter determines feasibility of the concept and gives a green light for systems design and further payload development.

The HYPSO mission objectives are as follows:

1) To provide and support ocean color mapping through a Hyperspectral Imager (HSI) payload, autonomously processed data, and on-demand autonomous communications in a concert of robotic agents at the Norwegian coast.
2) To collect ocean color data and to detect and characterize spatial extent of algal blooms, measure primary productivity using emittance from fluorescence-generating micro-organisms, and other substances resulting from aquatic habitats and pollution to support environmental monitoring, climate research and marine resource management.
3) Develop robust framework for rapid systems engineering for a pipeline of spacecraft that may optimize project development in academia and industry.
4) Build strong competence and strengthen the prospect of nano- and micro-satellite systems as supporting intelligent agents in integrated autonomous robotic systems dedicated to marine and maritime applications in Norway and internationally, these being applicable to communications and remote sensing (altimetry, SAR, radiometry etc.).
5) Describe scientific methodology that will be adopted for the research, and coordinate the project plans with other ongoing research activities at NTNU and other research institutions and companies.

Furthermore, it is emphasized that this mission is developed by PhD students, researchers, Master's students and professors, hence it shall be of academic nature and include objectives to emanate publishable results in the respective domains of control theory, artificial intelligence, electrical engineering, aerospace engineering, marine technology, biology and remote sensing.

Given the objectives it is important to establish a Level-0 statement for the mission:

HYPSO mission shall, through narrow field-of-view push-broom Hyperspectral Imaging, demonstrate proof-of-concept oceanographic observations dedicated to ocean color remote sensing by intelligently supporting

a concert of robotic agents consisting of UAVs, USVs, AUVs and stationary buoys observing the same target areas.

The Level-0 mission statement flows down to success criteria and consequently to the functional and operational requirements in Appendix A. The success criteria are operational in nature may be considered a minimum or full success depending on the operations after launch. System requirements follow from mission non-functional requirements.

A. Mission Architectures

With the concept defined in previous section, it is important to establish how operations will function in practice. The concept expands into an architecture represented by a functionality tree constituted by sub-elements. Listing trade-offs for each mission element, one may construct architectures that differ in the properties and technicalities thus having varying impacts on cost, design and operations as function of design solutions. The most important mission elements are listed as follows: A = Mission Concept; B = Controllable Subjects; C = Passive Subject; D = Payload; E = S/C bus; F = Orbit; G = Launch; H = Ground System; I = Communications Architecture; J = Mission Operations. Table II shows the options for each mission element selected, although these are kept open for an abundance of alternatives. Baseline elements are indicated with number 1 and orange text signifies alternatives to baseline solution.

All these combinations of mission elements give 40 mission architectures. The elements are highly correlated, therefore justifying the need for detailed unbiased decision criteria analysis. System drivers are rated towards each mission element, more specifically, drivers that impact the outcome of a decision for an architecture. Drivers such as program cost, risk, mission reliability, development reliability, man-hours, science output and size of data rate are weighted highest across a normalized scale. The drivers and mission elements are fed into a black box, or Decision-Making Analysis, i.e. *TOPSIS* or *AHP* as shown in Fig. 5 [11], [12]. These "black-box" methods select the most reliable candidates of mission architectures, ranking them as shown in Table III. The top 5 architectures are chosen to investigate here and will be iterated on further until choosing only one with confidence for detailed systems design and an eventual launch.

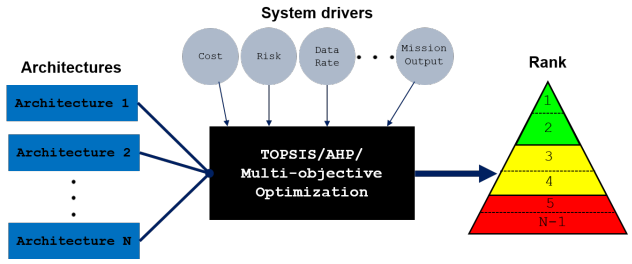

Fig. 5. Input to decision making 1st order or multivariable algorithms with rank driven by system drivers

TABLE II
MISSION ARCHITECTURES

Element	Option
A1	HSI mapping of the ocean; autonomous onboard processing of mission data, then transmitted after pass; ground commands on mission plan.
A2	HSI mapping of the ocean; autonomous onboard processing of mission data, then transmitted after pass; ground commands on mission plan; updates to other robotic agents.
A3	HSI mapping of the ocean; semi-raw downlinked mission data, then post-processed; ground commands on mission plan.
A4	HSI mapping of the ocean; semi-raw downlinked mission data, then post-processed; ground commands on mission plan; if satellite sees interesting signature → send out other air/surface agents directly
A5	HSI mapping of the ocean; autonomous onboard processing of mission data, then transmitted after pass; ground commanding on mission plan; autonomous coordinated robotic multi-agent observations
B1	No agents tracked from space
B2	Multi-agent targets tracked: USVs, UAVs, Ships, Buoys
C1	Oceanography through Hyperspectral imaging
D1	Small aperture HSI
D2	SDR
E1	2-6U size; 3-axis stabilization; spacecraft pointing; body-mounted solar panels; onboard GPS; onboard orbit control; possibly micro-propulsion
F1	SSO; 1-satellite
F2	(P)LEO; 1-satellite
G1	PSLV or Soyuz 9 (highly tradeable)
H1	Dedicated: NTNU; Commercial (e.g. KSAT)
I1	Store & dump data; TM/TC-transceiver; ≥2 ground stations; UHF-band uplink, X-band downlink
I2	Store & dump data; TM/TC-transceiver; ≥2 ground stations; UHF-band uplink, S-band downlink
I3	Store & dump data; TM/TC-transceiver; ≥2 ground stations; S-band uplink, X-band downlink
I4	Store & dump data; TM/TC-transceiver; ≥2 ground stations; S-band uplink, S-band downlink
I5	Store & dump data; TM/TC-transceiver; ≥2 ground stations; UHF-band uplink, X-band downlink; multi-agent cross-links in VHF/UHF
I6	Store & dump data; TM/TC-transceiver; ≥2 ground stations; UHF-band uplink, S-band downlink; multi-agent cross-links in VHF/UHF
I7	Store & dump data; TM/TC-transceiver; ≥2 ground stations; S-band uplink, X-band downlink; multi-agent cross-links in VHF/UHF
I8	Store & dump data; TM/TC-transceiver; ≥2 ground stations; S-band uplink, S-band downlink; multi-agent cross-links in VHF/UHF
J1	Fully automated ground stations; part-time operations on demand; Indirect updates on mission to/from other agents
J2	Fully automated ground stations; part-time operations on demand; Direct updates on mission to/from other agents

TABLE III
TOPSIS DECISION RANKING

Rank	Mission Architecture
1	A3-B1-C1-D1-E1-F1-G1-H1-I2-J1
2	A1-B1-C1-D1-E1-F2-G1-H1-I2-J1
3	A3-B1-C1-D1-E1-F2-G1-H1-I1-J1
4	A3-B1-C1-D1-E1-F1-G1-H1-I2-J1
5	A2-B2-C1-D1-E1-F1-G1-H1-I6-J2

B. Science Requirements

Since the main driver for this mission is oceanography, specifically dedicated to narrow field-of-view monitoring and mapping of ocean color phenomena particularly linked to biology, the key science objectives are:

- Detect algae and phytoplankton in Case 1 and Case 2 waters with Chlorophyll-a (Chl-a) concentrations of at least 1 mg/m^3 (see Table IV for relevant biology)
- Enable <100 m pixel resolution and high spectral resolution of at least 10 nm to characterize useful signatures
- Detect color of other matter such as biology, color-distorted organic matter, oil spills and river plumes
- Distinguish harmful and non-harmful species cooperatively from space observations (inferral) and in-situ measurements (validation)
- Enable remote sensing corrections for atmosphere, aerosols, air bubbles, sun-glint, water turbidity, diffracted second order light, water vapor, landscape distortions
- In-situ validation of remote sensing data will be necessary by methods of using USVs, AUVs or manual sample collection
- Space remote sensing shall be coordinated with NTNU AUV field campaigns in Svalbard, Trondheim and Frøya
- Positive detections of relevant signatures from space are to be investigated closer by UAV, USV or AUV with high response
- Observations shall be available in Spring/Summer time from March to July when biology is relatively abundant and probability of detection is highest

One of the main phytoplankton classes that are common in Norwegian ocean are a) Diatoms; b) Prymnesiophytes; c) Raphidophytes/Dictyochophytes; d) and Cyanophytes aka Cyanobacteria [5]. Algae/plankton classes and species to look for in Norway/Scandinavia are listed in Table IV.

C. Payload Requirements

Some selected payload requirements needed to fulfill the mission requirements and science objectives are as follows:

- Faintest detectable ToA signature for on-board algorithm detection shall be at least SNR of 200:1 in the range of 400-600 nm range and at least SNR of 50:1 in the 600-800 nm range
- Onboard processing shall consist of automated geometric (situational awareness) processing/calibration; radiometric processing/calibration; spectral compression; and spatial compression in the respective order and have feedback loop to the navigational and control & task execution data from ADCS
- Corrections for atmospheric distortions, water particles, aerosols, turbidity, clouds shall be enabled by utilizing $750-800$ nm (NIR) bands
- Four imaging modes shall be enabled: 1) high-resolution with 100 spectral bands; 2) medium-resolution with 100 spectral bands; 2) high-resolution with 20 spectral bands; 3) medium-resolution with 20 spectral bands
- On-board super-resolution or deconvolution algorithms shall enable overlapping fields of view to be fused in order to enhance the image resolution by a factor of at least 3 and mean SNR of at least $\sqrt{3}$
- Level 2 data transmitted to ground shall consist of geometrically and radiometrically calibrated and geo-referenced hyperspectral images with up to 100 spectral bands and $\leq$ 10 nm resolution that have Gaussian average for each band
- Level 4 data transmitted to ground shall consist of target location and at least radiometrically calibrated hyperspectral images with up to 20 spectral bands and ≤ 5 nm resolution that have Gaussian average for each band
- Payload shall operate in unique modes according to the database used (e.g. gain tuning, exposure time, binning operations, and spectral compression)
- Payload shall enable on-board radiometric and geometric calibration resulting in $\leq 15\%$ radiometric uncertainty and ≤ 10 % geometric uncertainty
- Payload shall work at medium to full processing power during two phases 1) image acquisition and 2) image processing during main target acquisition, and be idle during other phases
- Non-mission-baseline payload operations shall be at low or medium intensity for imaging and data processing

D. Orbit Selection

The orbit is selected given a preferred observation target in the coast of Mid-Norway and prospective Ground Stations in Trondheim and Svalbard for communications. Orbit parameters are summarized in Table V. A sun-synchronous orbit is chosen which is a near-polar orbit with inclination $i = 96-98^\circ$ and altitude $h = 500-800$ km. The advantage is that the satellite passes over any given point of the Earth's surface at the same local sidereal time, however J2 effects or oblateness of the Earth will precess the nominal RAAN, Ω, but less as compared to a polar orbit. The orbit is chosen such that at least approximately 60% of the orbit is in constant sunlight and other 40% in Earth's shadow (Umbra) in order to meet the mission requirements to observe a target off the coast of central Norway during morning or mid-day. This gives $\Omega = 15-35^\circ$ (south-to-north pass during the day) or $\Omega = 260-280^\circ$ (north-to-south pass during the day).

1) Targets: Baseline targets to be observed are: a) Frøya; b) Barents Sea (North of Finnmark County); c) Baltic Sea; d) Lofoten; e) Azores & Portugal; f) Monterey Bay; g) Lake Hudson; h) East Greenland; i) Svalbard. All of these regions have significant history of algal blooms and appearance of non-nominal ocean color and biology and are therefore of interest to observe. Specifically, Frøya, Barents Sea, Lofoten and Svalbard are interesting to observe from space in order to support AUV field campaigns (sampling and underwater imaging) run by NTNU regularly [2].

[2] HYPSO may, through mission control communications, aid AUVs by directing them towards corrected coordinates based on what the satellites sees which will significantly save both operational costs and time.

TABLE IV

AVAILABLE BIOLOGY IN NORWAY/SCANDINAVIA

Class	Color	Location	Season
Diatoms	Green/yellow	S to Mid-West Norway	Mar-Jun
Prymnesiophytes	Golden/brown	All Norway	Apr-Jul
Raphidophytes/Dictyochophytes	Golden/brown	South-West Norway	Apr-May
Cyanophytes	Reddish	Baltic/Skagerrak/South Norway	Jul-Sep
Species (red = TOXIC)	Color	Location	Season
Skeletonema costatum	Golden/brown	Skagerrak	May-Jun
Chaetoceros convolutus	Golden/brown	Rogaland-Helgeland	Mar-Apr
Prymnesium parvum	Golden	Hylsfjord in Ryfylke	Jul-Aug
Chrysochromulina polylepis	Brown	S, SE, W and Mid-Norway, Oster/Sørfjord	Apr-Jul
P. papilliferum	Golden	Hylsfjord in Ryfylke	Jul-Aug
Heterosigma akashiwo	Reddish	Osterfjord/Sørfjord	Apr-May
Karenia mikimotoi	Golden/brown	Skagerrak/Baltic	Apr-Aug
Karlodinium veneficum	Golden/brown	Skagerrak/Baltic	Apr-Aug
Emiliania huyxlei	Milky/brown	Along all Norwegian Coast	Apr-Sep
Pseudochatonella	Golden/brown	Baltic	Apr-Aug

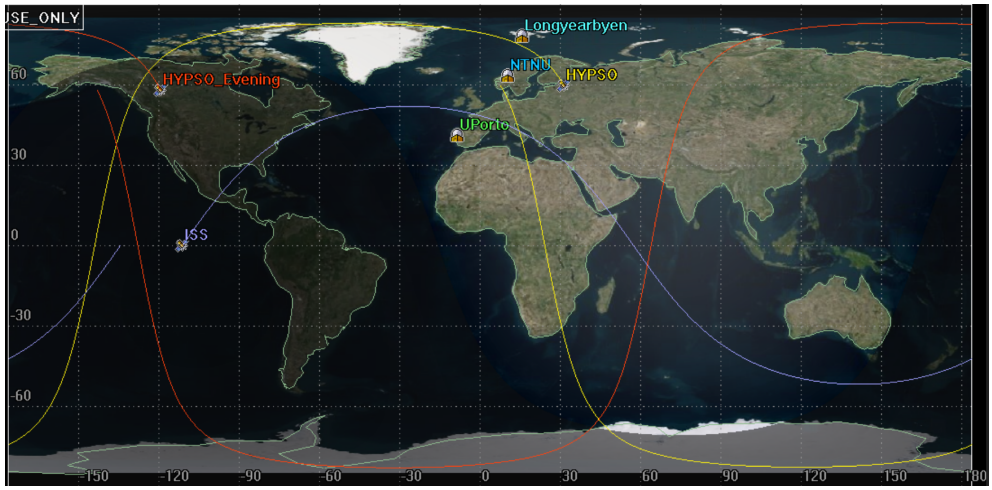

Fig. 6. Groundtrack HYPSO in morning, evening and ISS orbits at epoch 16 May 2018 07:00:00 (UTC).

TABLE V

BASELINE ORBIT CONFIGURATION

Orbit Parameter	Value
Launch LTAN	10:00 AM/10:00 PM
Semi-major axis, a	6878 km
Altitude, h	500 km
Average altitude loss	-3.4 m/day
Speed, v_{sat}	7.621 km/s
Orbit period	94 min 49 s
Inclination, i	97.31°
Eccentricity, e	0.0015
RAAN precession rate	3.6×10^{-5} °/day westwards
Angular momentum	52261.69 km^2/s
Revolutions	15.31 revs/day
Repeat cycle	7 days
Mean eclipse ratio	36.1 %
Lifetime	6.7 years

2) Orbit Configuration 1: Parameters for a morning SSO configuration are $h = 500$ km, $i \approx 97.31°$ and LTAN 10:30 AM at launch, and is called a "morning" orbit since the Right Ascension of Ascending Node (RAAN) crosses the equatorial plane in the morning 10:00 AM (LTAN). Figs. 6 and 7 show a SSO SmallSat configuration ground track and 3D view, respectively. Note that the Norwegian coast is covered several times per day (both northwards and southwards passes as Earth revolves about its axis), although the orbit track does not give the satellite flexibility in observing along the coast since it passes Norway cross-track to the coast. Ground track repeat cycle is about 7 days for this configuration. Details about access times to selected targets and Ground Stations are given in Table VI, , where blue indicates ground station and red indicates target to image. It is assumed that target areas and ground stations have elevation angles of $\epsilon_{\text{Target}} = 20°$ and $\epsilon_{\text{GS}} = 10°$ respectively where first is due to optical viewing angle constraints ($\gamma < 70°$).

TABLE VI

ACCESS TIMES (16 MAY 2020 07 AM - 17 MAY 2020 07 AM) FOR CONFIGURATION 1

	NTNU	Svalbard	UPorto	Frøya	Barents
# passes	7	11	2	3	4
Max (min)	7.408	7.478	7.446	5.011	5.517
Mean (min)	5.478	6.813	7.315	3.397	3.997
Min (min)	2.780	4.743	7.185	1.888	0.928

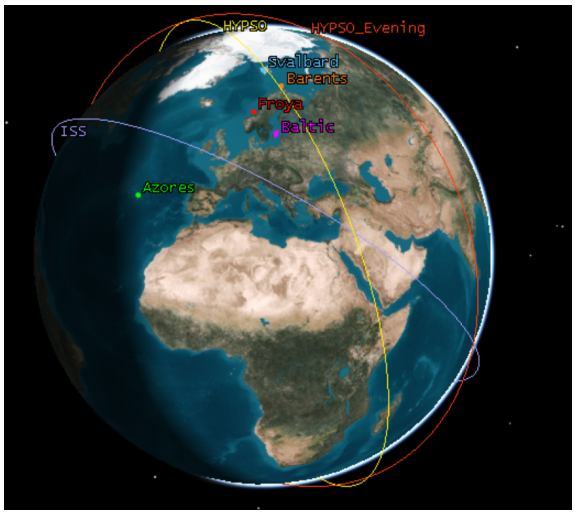

Fig. 7. Two possible HYPSO orbits (SSO) at altitude $h = 500$ km and ISS orbit.

3) Orbit Configuration 2: Second configuration has $h = 500$ km, $i \approx 97.31°$ and 10:00 PM LTAN, which is called an "evening" orbit. Figure 7 shows the particular orbit configuration where the satellite, at this particular time of the year, goes from north to south. Note that the Norwegian coast is covered several times per day. One particular orbit may potentially pass all the way from Svalbard down to the tip of Southern Norway, covering the whole coast. Appropriate launch window must be chosen wisely to avoid sun glare effects though these are fewer than in morning. Since many biological events happen in the Spring around 10 AM, this orbit appears more scientifically viable as it offers flexibility along observing the whole coast. Ground track repeat cycle is about 7 days also for this configuration.

Details about access times to NTNU, Longyearbyen, UPorto, Frøya and Barents are given in Table VIII where blue indicates ground station and red indicates target to image.

TABLE VII
ACCESS TIMES (16 MAY 2020 07 AM - 17 MAY 2020 07 AM) FOR CONFIGURATION 2

	NTNU	Svalbard	UPorto	Frøya	Barents
# passes	6	11	4	2	5
Max (min)	7.405	7.446	7.182	5.005	5.350
Mean (min)	5.725	6.484	5.375	3.835	4.507
Min (min)	2.349	3.460	2.871	2.665	3.471

4) Backup Orbit: Constraints due to costs and budgets may have an impact on the project development and hence result in a less desirable but affordable orbit that are accessible with cheaper launches. For instance launches are most abundant and frequent to ISS due to high-demand for supply, maintenance and rapid science measurements on the space station. ISS is also at a lower altitude and low inclination of $i \approx 51.6°$, hence launcher costs are lower. This backup orbit is also analyzed in case of an orbit insertion/deployment going wrong for a nominal SSO launch where it is stipulated in the worst case that HYPSO will have a low inclination hence access is not granted to either NTNU, Svalbard or nominal target areas in Frøya, Baltic and Barents Sea. Figures **??** and **??** show the ground track and orbit, respectively. Details about access times to selected targets and Ground Stations are given in Table VI, where blue indicates ground station and red indicates target to image.

TABLE VIII
ACCESS TIMES (16 MAY 2020 07 AM - 17 MAY 2020 07 AM) FOR ISS CONFIGURATION

	UPorto	UVigo	Monterey	Azores	Cape Point
# passes	7	7	1	1	3
Max (min)	6.554	6.581	3.963	4.390	4.221
Mean (min)	4.740	4.839	-	-	2.706
Min (min)	3.340	2.723	-	-	0.558

5) Launcher: A few candidates for launch are:

- PSLV (ISRO)
- Falcon-9 (SpaceX)
- Soyuz-2 (Russia)
- Ariane 6 (Arianespace)
- Antares (Orbital ATK)
- Pegasus (Orbital ATK)
- Electron (Rocket Lab)

For instance for the Falcon-9 (SpaceX) launcher, some requirements are that HYPSO must structurally and mechanically endure:

- Axial acceleration of 6 g's
- Lateral acceleration of 2 g's
- Fundamental axial frequency of 25 Hz
- Fundamental radial frequency of 10 Hz

IV. HYPERSPECTRAL IMAGER (HSI) PAYLOAD

The HSI design is based on a grating spectrograph (without prism). Components are mainly commercial off-the-shelf from Thorlabs.com and Edmund Optics, except for the grating holder which may be 3D printed. The detector is an industrial camera head from The Imaging Source Europe GmbH. sensor used is the CMOS image sensor Sony IMX147. A 300 grooves/mm transmission grating is blazed at 17.5° with efficiency above 50% for 400-800 nm spectral range. The aperture is 24 mm with an input F/value equal to 2. The input slit width is adjustable with no magnification of the slit height ($\tilde{h}_{\text{slit}}$ = 7.032 mm). A slit width of w_{slit} = 25 μm will result in a spectral bandpass (FWHM) of approximately 1.67 nm without binning. Fig. 8 shows the layout of an optical diagram which visualizes a center cross-section of the instrument, parallel to the refraction axis. The current HSI V6 prototype (Version 6) is depicted in Figure 9. Table IX provide the optical dimensions related to Fig. 8 for the current HSI (version 4.1) and proposed space HSI (version 4.2). Further specifications are given in Table X that describe the HSI performance. Table XI offers spectrometer designs that are different but may achieve same goals as the HSI version 6.

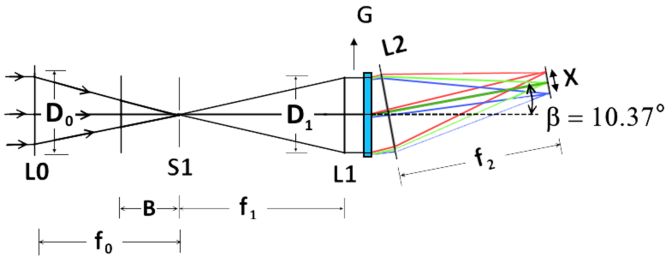

Fig. 8. Optical diagram of Spectrometer. L_0 is the front lens with lens diameter D_0, f_0 is the focal length between L_0 and entrance slit S_1, B is the back focal length, f_1 is the focal length between entrance slit S_1 and collimator lens L_1 with diameter D_1, G is the grating with lens L_2, f_2 is the focal length between the grating G and the detector X. The light dispersion angle is $\beta \approx 10.37°$. Credit: Fred Sigernes.

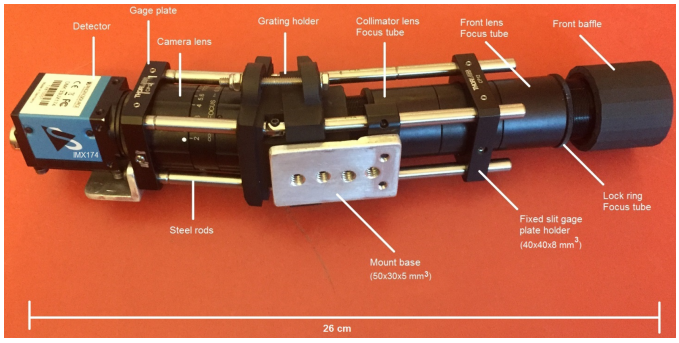

Fig. 9. Current HSI version 6. Credit: Fred Sigernes.

A. Electronics

The goal of the PCB is to get the entire processing chain up and running with image sensor and on-board processing, and to get a better understanding of the challenges involved in hyperspectral imager hardware development. The HSI will be mounted on a 9.4× 9.4 cm PCB with FPGA processing unit for onboard data handling and image processing. The PCB, as shown in Figure 10, is based on using an ARM/FPGA (Zynq7000) computer and has average power consumption $<$ 3 W. The sensor supports up to 100fps with a 12-bit resolution of images. It also supports multiple protocols across its processors.

TABLE IX
HSI VERSION 6 OPTICS DIMENSIONS

Part	Dimensions	Description
$f_0/\#$	$f_0/2$	f-number front lens
$A_0(L_0)$	24 mm	Aperture front lens
f_0	50 mm	Focal length front lens
B	8.6 mm	Back-flange focus
w_{slit}	25 μm	Entrance slit width
h_{slit}	10 mm	Entrance slit height
$\tilde{h}_{\text{slit}}$	7.032 mm	Effective entrance slit height
$f_1/\#$	$f_1/2$	f-number collimator lens
$A_1(L_1)$	25 mm	Aperture collimator lens
f_1	50 mm	Focal length collimator
G	25 × 25 mm^2	Grating area
$A_2(L_2)$	25 mm	Aperture grating lens
$f_2/\#$	$f_2/2$	f-number detector lens
f_2	50 mm	Focal length detector lens

TABLE X
HSI VERSION 6 PERFORMANCE SPECIFICATIONS

Mass m	544 g
Volume	80 × 60 × 220 mm
$iFoV$	0.0286° × 8.4485°
Total optical efficiency η_{OE}	$0.8^3 \approx 0.5$
Cross-track pixels N_y	1200 pixels
Grating	300 grooves/mm
Grating efficiency η_{G} 500 nm	73 %
Sensor	Sony IMX174 1920 × 1200 pixels
Spectral range	400-800 nm
Bandpass $\Delta\lambda$	1.67-10 nm
Pixel size $p_x \times p_y$	5.86μpixels × 5.86μpixels
Binning	Up to 10×
Usable bands	100
Quantum efficiency η_{QE} 500 nm	77 %
Dark current	0.95 e^-/s
Read-out noise (25 C°)	7 e^-
@ altitude h = 500 km	
Exposure time Δt	32.8 ms
Swath width	70.32 km
δx	250 m
Δx	500 m
Δy	58.6 m
v_{sat}	7.6127 km/s

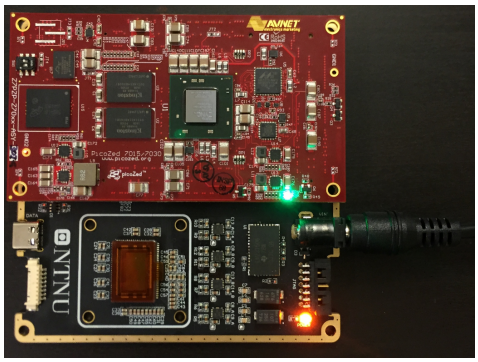

Fig. 10. PCB developed for the HSI to be mounted 2.5U in HYPSO . The image sensor used here is a CMOSIS CMV2000.

Specifications for the PCB are

- Storage: 36GB (4GB eMMC + 32GB microSD)
- Memory: 1GB
- Processor: Dual Core ARM A9 (Zynq 7030 Series FGPA)
- Input Voltage: 4.5-14.5V
- Maximum current: 6A
- Connectivity: USB 2.0, UART

The data is read out using low voltage differential singling (LVDS) and controlled using SPI. For maximum quantum efficiency, the variation of the sensor processed on 12 μm epitaxial (E12) SI wafer is used. The thicker epic-layer increases the sensitivity to light above 600 nm significantly. Due to the sensitivity due to high speed data transfer, the data lines are carefully impedance matched following the TIA/EIA 644 standard for LVDS signals.

B. Performance

The spectral bandpass is given as, where $a = 3333.33$ nm is the groove spacing. Spectral order is $k = 1$ and incident angle $\alpha = 0$. If the slit width is $w_{\text{slit}} = 25\mu$m then $BP = 1.67$

TABLE XI
OTHER SPECTROMETER DESIGNS

Type	Description
PRISM "Dyson" [13]	Considered the "best" dark target pushbroom hyperspectral prototype to consider, combining low f-number, low internal scattering, and low monochromatic and chromatic aberrations to maximize SNR over dark targets.
Offner [14]	Three-concentric-mirror (Offner) configuration. The approach presented allows for the rapid design of this class of system.
CHAI V-640 [3]	Commonly used airborne sensor for validation campaigns for remote sensing (satellite hyperspectral imagery)
NovaSol [4]	Airborne hyperspectral design but possibly at larger form factor

nm. The effective slit height is $\tilde{h}_{\text{slit}} = 7.032$ mm. This is the height of the Sony IMX174 CMOS detector.

Since the satellite will be in a sun-synchronous orbit at $h \approx 500$ km altitude, the FoV at Nadir may be calculated as follows:

$$iFoV = \tan\frac{w_{\text{slit}}}{f_0} \times \tan\frac{\tilde{h}_{\text{slit}}}{f_0} \tag{1}$$

giving $iFoV = 0.0286° \times 8.4485°$ (in-track $\times$ cross-track). This results in larger pixels along the direction of flight as compared to lower altitudes, and defines the spatial resolution as illustrated in Fig 11. The distance δx defines the ground segment optical resolution as seen by the instrument at time $t = t_0$ and is the instantaneous ground resolution expressed as,

$$\delta x = \frac{h w_{\text{slit}}}{f_0} \tag{2}$$

Raw instantaneous sampling is illustrated in Fig 12. The spatial resolution may be calculated as,

$$\Delta x = \delta x + v_{\text{sat}} \Delta t \tag{3}$$

where $\Delta t = t_1 - t_0$ is the exposure time and v_{sat} is the speed of the satellite. It does not include the read-out time τ for the sensor. The criterion for read-out time may be determined as,

$$\tau \leq \left(\frac{h w_{\text{slit}}}{f_0 v_{\text{sat}}}\right) \tag{4}$$

Cross-track to the flight direction the resolution is calculated simply as

$$\Delta y = \frac{h \tilde{h}_{\text{slit}}}{f_0 N_y} \tag{5}$$

where N_y is the effective number of pixels along the slit image.

For exposure time of $\Delta t = 32.8$ ms (read-out time should be less than or equal to this), 31 frames per second ($1/(\Delta t) \approx 31$ fps) and the HSI specs f_0 =50 mm, $w_{\text{slit}} = 0.25\mu$m, $f/2$ and $N_y = 1200$, this gives δx =250 m, Δx =500 m, Δy =58.6 m and swath width $SW = 70.32$ km. The number of pixels per spectral bin is 4.3 pixels for BP = 1.67 nm using the Sony IMX174 CMOS as sensor. If we bin by a factor of 4 along the slit height, we will obtain close to square image pixels mapped to an area of 234.4 $\times$ 250 m^2 at ground level. Binning 13 pixels in the spectral direction will result in an image bandpass of 5 nm. This will increase the image throughput and does not affect the spatial resolution of the end image. The number of pixels per spectral bin is 4.7 pixels for BP = 1.67 nm using the CMOS UI-3360CP-NIR as sensor. Swath Width is $SW = 59.84$ km and Δy =51.875 m for this sensor.

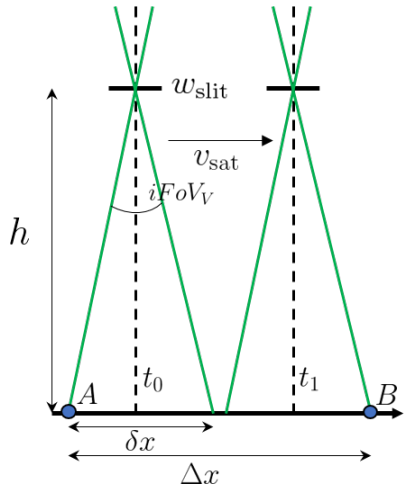

Fig. 11. Field of view of slit as satellite moves with velocity v_{sat} and h is altitude above ground level. The spatial resolution then becomes equal to the distance from point A to B denoted as Δx.

C. Signal-to-Noise Ratio

This section covers the sensitivity analysis of optics performance to determine feasibility of the sensor and image acquisition from Low-Earth-Orbit (LEO) at $h = 500$ km. The methodology is based on relevant calculations from Ocean Optics Website[5] and a RESONON white paper on SNR[6]. It can be seen in Fig. 13 that significant atmospheric disturbances increases with altitude but not much more over 30 000 m. Radiances in Wm^{-2}sr^{-1}nm^{-1} are modeled with the following MODTRAN inputs as assumptions that were run in Hydrolight Software:

- cloudless mid-latitude summer atmosphere
- marine aerosols present
- relative humidity of 76% at sea level
- solar zenith angle of 50°
- surface wind speed of 6 m/s
- Nadir-viewing sensor ($\gamma = 0°$)
- horizontal visibility of 63 km
- homogeneous water

[5] http://www.oceanopticsbook.info
[6] https://www.resonon.com

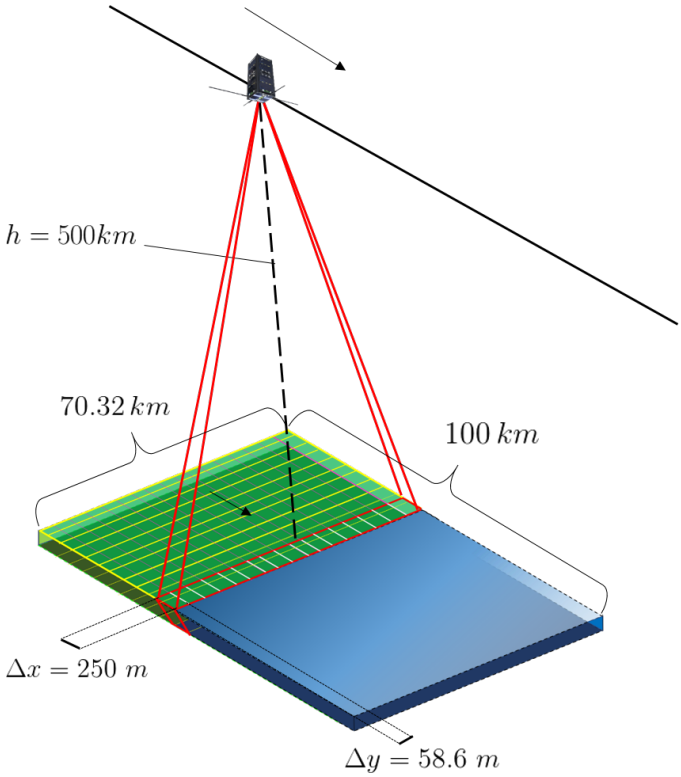

Fig. 12. Nadir mapping of 100 × 70.32 km^2 target area with optical resolution $\delta x = 250$ m.

- Case 1 water with Chl-a concentration of 1 mg/m^{-3}
- infinitely deep water

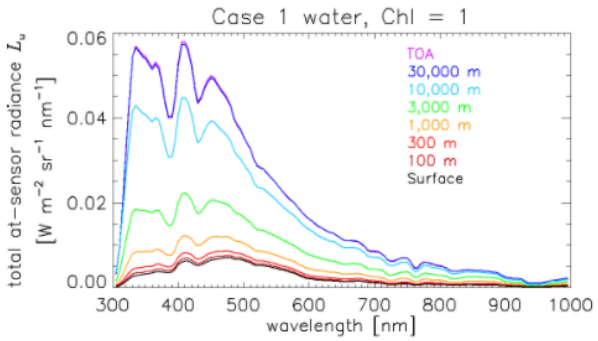

Fig. 13. Example generated (from HydroLight software) radiances L_u for different HSI sensor altitudes with Case 1 water and Chl-a concentration of 1 mg/m^3 which is pretty low. The water-leaving radiance and surface-reflected radiance (not shown) are the same in all cases. Shows significant atmospheric disturbances with increasing altitude. Reference: `http://www.oceanopticsbook.info`

The radiances are re-run in HydroLight software for spectral range of 400-800 nm with spectral resolution of 5 nm in Figure 14.

One of the parameters to understand the performance of the camera with respect to a desired signal or photons reaching the sensor is to determine the signal-to-noise ratio (SNR). The constants for the HSI are required to determine photon count as shown in Tables IX and X.

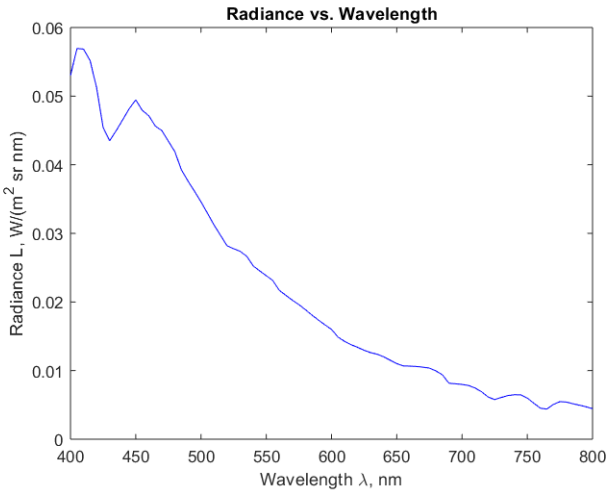

Fig. 14. L_u reaching the HSI sensor in-situ and top of atmosphere (ToA) which determines amount of photons detected at each spectral band with $\Delta\lambda = 5$ nm. Reference: `http://www.oceanopticsbook.info`.

The sensor and grating efficiencies at each wavelength are shown in Figure 15.

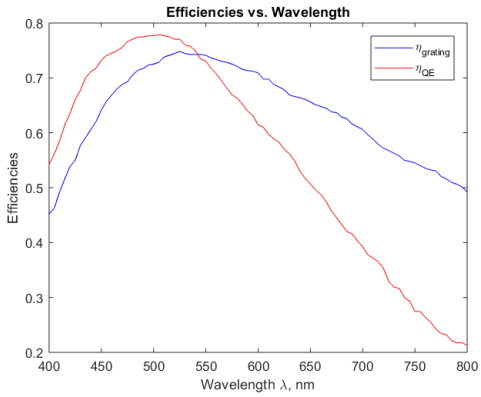

Fig. 15. Efficiencies to be expected for grating and HSI sensor SONY IMX174 across the spectral range.

The effective slit width may be written as

$$\tilde{w}_{\text{slit}} = w_{\text{slit}} \cos\alpha / \cos\beta = 2.5415\mu m \tag{6}$$

Knowing that the pixel size is $p_x = 5.86\mu$m, then the area on the detector per pixel can be calculated as

$$\tilde{A}_{\text{detector}} = \tilde{w}_{\text{slit}} p_x = 2.5415\mu m \tag{7}$$

Assuming viewing angle $\gamma = 0°$, the solid angle of the sensor at Nadir as seen from the earth's surface is

$$\Omega_{\text{aperture}} = \frac{\pi(A_0/2)^2}{r^2} = 4.9087 \times 10^{-16} sr \tag{8}$$

where r is the range and $r = \frac{h}{\cos\gamma} = h$. Entendue is then calculated as

$$E_{\text{aperture}} = \frac{\pi A_0 \cos\alpha}{4 f_0^2} w_{\text{slit}} \tilde{h}_{\text{slit}} = 1.3807 \times 10^{-6} cm^2 sr \tag{9}$$

If we assume a selected wavelength of $\lambda = 550$ nm, the corresponding number of photo-electrons released in the detector in time $\Delta t = 0.0328$ seconds is

$$N_{\text{electrons}} = \frac{\pi L \tilde{A}_{\text{detector}} \Delta\lambda \Delta t \eta_{\text{G}} \eta_{\text{OE}} \eta_{\text{QE}} \lambda}{4(f_0/A_0)^2 + 1) h_{\text{planck}} c} = 1.0491 \times 10^5 \tag{10}$$

where L is the irradiance reaching the front lens at Top of Atmosphere for $\lambda = 500$ nm, h_{planck} and c are Planck's constant and speed of light, respectively. The exposure time $\Delta t = 0.0328$ determines how much the satellite sees in a movement of $v_{\text{sat}} \times \Delta t = 250$ m, i.e. spatial resolution of $\Delta x = \delta x + v_{\text{sat}} \times \Delta t = 500$ m at Nadir. Of a total of 1.0491×10^5 photon-electrons, 1.0491×10^4 water-leaving photon-electrons reach the sensor due to the atmospheric effects shown in Figure 14. Approximately 5-10 % of total ToA photons consists of water-leaving photons. Using the numbers from Tables IX and X, the SNR is calculated as follows,

$$SNR = \frac{N_{\text{electrons}}}{\sqrt{N_{\text{electrons}} + B i_{\text{dark}} \Delta t + B e^2_{\text{read}}}} = 323.7 \tag{11}$$

where B is number of binning operations. It is assumed that binning operations are $3\times$ that are incorporated into achieving spectral resolution of $\Delta\lambda = 5$ nm. With SNR of 323.7 at 550 nm, it can be estimated that the SNR of water-leaving radiance will be ≈ 32.

Figure 16 shows the sensitivity of SNR to front lens aperture size (A_0)

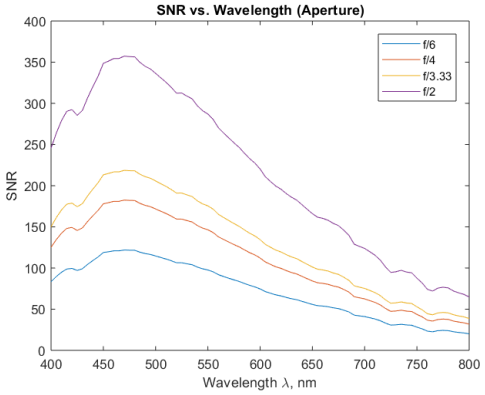

Fig. 16. SNR vs. aperture, clearly showing increase in SNR as aperture of lens increases.

Figure 17 shows the sensitivity of SNR to exposure time Δt. The main compromise here will be between spatial resolution and signal strength due to number of frames taken per second.

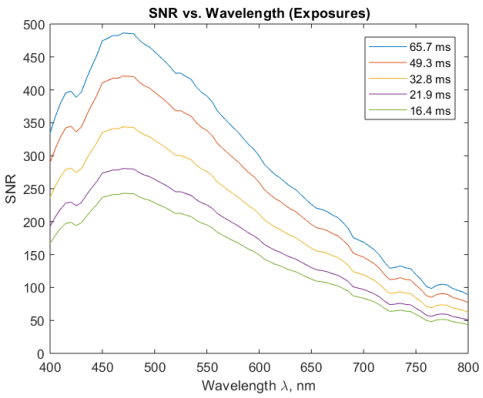

Fig. 17. SNR vs. exposure time, clearly showing increase in SNR as exposure time becomes longer.

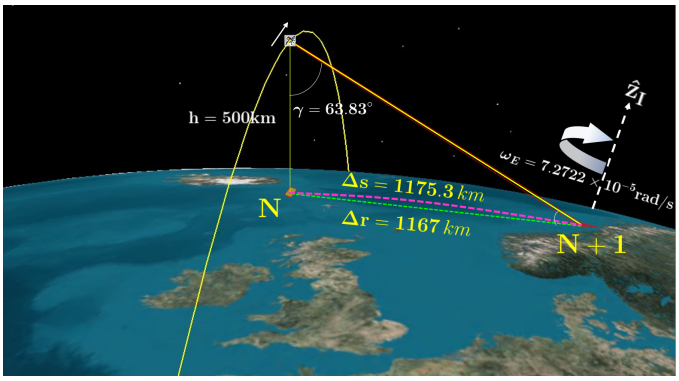

Fig. 18. SmallSat at $h = 500$ km in two consecutive passes with ≈ 95 minutes period, where $N+1$ pass shows the target area (same ground point) has moved approximately 1175 km at latitude of $63.11°$, resulting a required $\Delta\gamma \approx 64°$ from Nadir in cross-track direction.

Pointing cross-track would be essential for narrow field-of-view imaging of targets that are off-nadir which would be a minimum requirement. To revisit the target and due to Earth's rotation, the spacecraft not only has to slew along-track but also point significanty in the cross-track direction given that the target area will move westwards in next pass. Two cases are to be considered:

- Figure 18 shows the example of the nominal pass where SmallSat at $h = 500$ km flies directly over the 50 long target, then needing to slew in the cross-track direction from Nadir, it can be shown that for the next pass after 95 min, the SmallSat would have to point to $\gamma \approx 64°$ due to the target that has moved 1175 km westwards.
- If the nominal SmallSat pass is right in the middle of the target in first and second pass then SmallSat would have to point to $\gamma \approx 45°$ wrt. Nadir due to the target having moved 588 km westwards.

Both the cases can be improved based on altitude selection and independent camera pointing. However, spatial resolution will also worsen, since along-track spatial resolutions are a function of slant range $r = h/\cos\gamma$. The slant range and increases with larger viewing angles hence ground pixels

become much larger and resolution of the target worsens. For $\gamma = 64°$, then $r = 1140.6$ km, $\delta x = 570.3$ m, $SW = 1604.1$ km and $\Delta y = 133.67$ m. Pointing requirements also need to be strict to avoid considerable motion blur and geometrically inconsistent pixels in the frame, typically giving less than 100 m error in order to achieve image resolution to be higher than 100 m.

Furthermore, the water-leaving radiance is related to the the phase function (assuming the water radiance is scattered by Lambertian BRDF) i.e.,

$$p(\gamma) = \frac{2}{3\pi^2} \left(\sin\gamma + (\pi - \gamma)\cos\gamma\right) \tag{12}$$

thus the reflected radiance from the water surface scatter and decrease when S/C views the target at larger angles.

D. Saturation

One way to avoid green saturation is to use an amethyst filter (e.g. `http://www.koppglass.com/filter-catalog/purple-filter-glass.php`) having a transmission curve that suppresses the green. Of course green signal is thrown away but at least can potentially improvement is made on the relative blue and red SNR while avoiding saturating the detector, which will likely render the whole frame indistinguishable; at best is to decimate the green part of the hypercube.

E. Stray Light

Stray light within the spectrograph may dominate the "noise" in the SNR problem. Any photon that does not reach the theoretically perfect place on the photodetector; that is the right row of color and the right column of cross-track location is called stray light. Sources include scattering/refraction from scratch and dig, stria, or cement flaws in the optics, monochromatic (Zernike) aberrations, chromatic aberration, polarization sensitivity, and non-ideal diffraction grating effects including scattering from ruling flaws, low diffraction efficiency (e.g. related to where the un-diffracted light goes), and poor order blocking filter performance. Characterization and correction schemes are given in [15].

F. Atmospheric Correction

Aerosols, gases, humidity, bubbles etc. distort the spectral response for a HSI. Figure 14 shows this effect, where 85-95 $\%$ of photons (depending on wavelength) are coming directly from the atmosphere. Since NIR is absorbed by the atmosphere (and water) more than VIS, many atmospheric corrections are employed using NIR [16], [17].

The advantages and challenges with HSI coastal observations in space are discussed briefly in [18]. The water-leaving radiance generally only accounts for around 10-15 % of the signal that may be observed in space, with the rest of the signal being corrupted by atmospheric and surface/landscape effects, especially for Case 2 waters being mostly coastal waters. It is noted that turbid waters and strong-absorbing aerosols occur in coastal waters which may bring challenges to remote sensing where NIR is necessary for these type of corrections. 700-800 nm may be used to discriminate clouds and land from the open ocean, as well as to map surface vegetation [18] such as on Coastal Zone Color Scanner (CZCS), launched by NASA in 1978.

Usage of HSI for high-sediment-loads observations (in VIS-NIR) is investigated by [19]. Spectral coverage to the shortwave-infrared (SWIR) region is useful for the estimation of suspended particulate matter (SPM) concentrations and for the correction of atmospheric contributions for remote sensing of coastal/in-land turbid waters. [20] also concludes with the necessity with NIR bands for proper atmospheric corrections, even for high Chl-a concentrations.

Hyperspectral Imager for the Coastal Ocean (HICO), mounted on ISS and retired in 2014, leveraged data to estimate Chl-a concentration in coastal waters, and was a successor to MEdium Resolution Imaging Spectrometer (MERIS). A further note on this is that it is common knowledge that MERIS superseded MODerate resolution Imaging Spectroradiometer (MODIS) given its band at 708 nm for estimating low-moderate Chl-a concentrations in turbid waters. HICO was a push broom sensor that captured data in the wavelength range 350-1080 nm, with a spectral resolution of 5.73 nm and GSD $\approx$ 90m. [21] presents the radiometric processing results and limitations using red-NIR models, as well as suggestions for future applications of spaceborne HSI in coastal waters. Again, high turbidity renders conventional blue-green algorithms unreliable for estimating Chl-a concentrations. To combat the optical complexity in such cloudy waters, algorithms for red and NIR regions of the spectrum have been recently developed and successfully validated for estimating Chl-a concentration in inland and coastal waters. HICO had problems with the red-NIR spectral range of 700-1080 nm due to contamination by diffracted second-order light in the wavelength range of 350-540 nm, from lack of an optical filter that would block out this second-order light. However there are empirical methods to alleviate this successfully [22], and by optical design [23]. The radiometric instability issue should be investigated further including the ability for onboard calibration (latter not possible for HICO). The visible light (400-700 nm) penetrates the water and provides information on water properties and bottom reflectance, and shortwave infrared radiation (700-900 nanometers) is used to correct for atmospheric aerosols and surface reflectance [16].

Hyperion, which was launched in 2000, has been used for coastal water studies. However, its SNR (50:1) was very low [24], and the sensor was unreliable in quantitatively estimating water quality parameters due to problems such as radiometric instability [25]. HICO, on the other hand has high SNR (200:1) over the visible wavelengths [16]. Even SNR of $> 200:1$ is achieved for NIR wavelengths, assuming 5 $\%$ albedo.

Spatial ground resolution of 100 m is recommended in order to characterize ocean coastal waters, and even higher resolution is required for high biodiversity of phytoplankton in certain coastal and inland waters [18]. LandSat for

instance, ”accidentally” proved useful for ocean color due to the high resolution, even though the application was not intended. [18] provides an overview of current and previous HSI flights as well as challenges.

Furthermore, [26] presents results using NIR bands for Chl-a concentration estimation from HICO and states that, apart from visible wavelengths for direct chlorophyll observations, shortwave infrared radiation (700-900 nm) is used to correct for atmospheric aerosols and surface reflectance [16]. It is especially important with these corrections for the retrieval of low-to-moderate Chl-a concentration.

Radiometric resolution datasheets on Sentinel-3 Ocean and Land Colour Instrument (OLCI) exist where the application of each spectral band is indicated[7]. OLCI is a push-broom imaging spectrometer with five cameras, where mitigation of sun-glint contamination is done by tilting cameras in westerly direction. Other specs for the OLCI are: swath width of 1270 km, spectral range of 400-1020 nm and spatial sampling of 300 m. From the datasheet it is evident what functionality each of the NIR bands have: 778.75 nm for atmospheric and aerosol corrections; 865 nm for atmospheric and aerosol corrections, clouds, pixel co-registration; 885 nm for water vapour absorption reference band and is the common reference band with SLSTR instrument, also used for vegetation monitoring; 900 nm for water vapour absorption/vegetation monitoring (max. reflectance).

See Fig. 19 for an overview of usage of the spectral bands in satellite missions. Several other techniques are

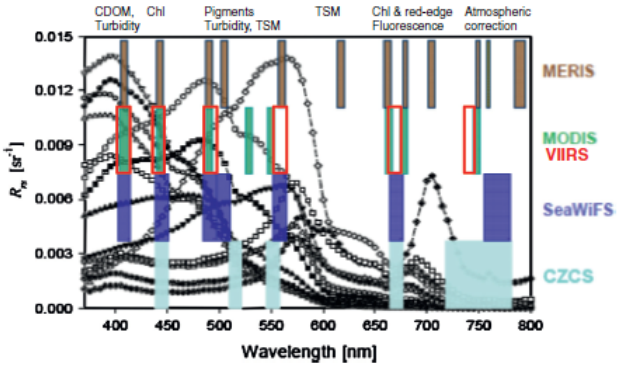

Fig. 19. Satellite missions with Multi-spectral Imagers and utilization of each spectral bands [17]

also envisaged to be investigated in contrast to the standard techniques in atmospheric correction. These involve using analytical algorithms based on the derivatives of the radiative transfer equation, termed as the derivative ratio algorithm [27]. A spectral shape algorithm that uses derivatives has been applied to Medium Resolution Imaging Spectrometer (MERIS) imagery that has detected cyanobacterial blooms, with extensive examples in Lake Erie [28]. The detection algorithm uses an approximation of the second derivative as a measure of spectral shape around the 681 nm band and has proven that these algorithms prove successful results without compromising the systematic noise in SNR.

[7]https://sentinel.esa.int/web/sentinel/user-guides/sentinel-3-olci/resolutions/radiometric

G. Calibration

Suggestions on calibration for HSI testbed to image the following (in order of priority):

1) Monochromatic light source, see if we can get the spectral response matching apriori knowledge of spectral band. Determine if sensor output spectral response is shifted from nominal. May use spectral photometer. 20 shows the 1st wavelength calibration performed on HSI V6.
2) Blue sky and characterize the spectral response as above in 1.
3) Black body source of light. Characterize spatial vs. spectral response. Characterize Quantization Efficiency at different wavelengths.
4) Diffuse source of light (e.g. water) - even illumination (not focused images)
5) Closing the camera cap to characterize dark noise, bias and read-out noise with different in exposure times based on camera specifications.
6) Any source of light (clean room) and subtract the noise to see signal response.

It is important to characterize Quantization Efficiency across wavelengths, edges of spectral range (400-900 nm) have lower quantization efficiency (vignetting). Additional noise comes from microbubbles (Rayleigh scattering) and also needs to be characterized (microbubbles most likely have noise described as random or by Brown distortion model).

One option is to take several images of a track and average those multiple images to estimate the noise in the camera and scene. Eventually one may determine PSNR for image reconstruction, also SNR to characterize image before and after reconstruction.

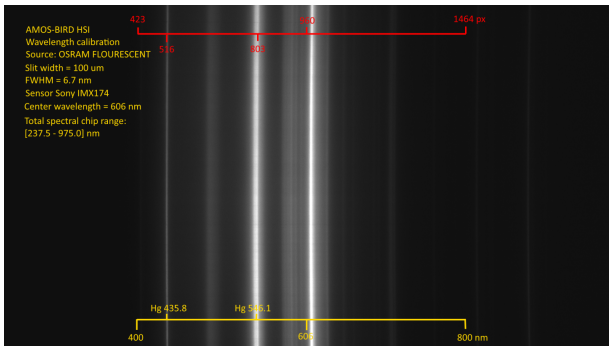

Fig. 20. 1st Wavelength calibration using the Imaging Source IMX174LLJ camera head. Source spectrum is office roof illuminated by an OSRAM FQ 54W/830 HO Fluorescence tube

H. Onboard Calibration

TBD

I. Performance summary

TBD. Summarize and compare the expected performance with Sentinel and planned HSI satellites ([7]).

V. HSI Data Processing and Control Architecture

Figure 21 illustrates information flow, integrated processing and control architecture. The layers from top to bottom correspond to the HSI payload with onboard processing, HYPSO bus within onboard task planning and control, ground control/operations with data and model management, and payloads and control on other assets such as UAV/AUV/USV and traditional satellite data products.

A brief description of the main functionality in the blocks in Figure 21 is given below:

- The **HYPSO HSI payload** and its On-the-Fly-Processing (OTFP) follows a processing chain that is similar to what is found in similar small satellite systems, e.g. [29]:
  - The **HSI data acquisition** block captures image frames that at each sampling instant has one spatial dimension (laterally, across the track) and one spectral dimension. The second spatial dimension (along the track) is built sequentially from these image frames as the satellite moves along. Predictions and observations of illumination (sun position and atmospheric conditions such as clouds) can also be used to optimize the attitude control and slewing in order to get the best possible data results given priorities within the target area.
  - In the **geometric image processing** block each pixel is transformed into a geographic location on the ocean surface. This is based on time synchronization of the image capture in the HSI data acquisition hardware, and measurements of attitude and position from the HYPSO's navigation system. Next, the data is re-sampled and arranged into a datacube with two spatial dimensions and one spectral dimension.
  - **Radiometric image processing** transforms each pixel value into absolute reflectance values. This involves a calibration process using models and measurements of the atmosphere, solar radiation and/or geo-referenced reference measurements near the ground. Pixel values that are occluded by clouds should be identified.
  - **Spectral image processing** is based on multivariate data modeling that projects the data onto expected and unexpected/observed "signatures" corresponding to the features of interest, [30]. This acts as a basis for data compression, detection of features, as well as removal of effects of specular reflections in the water, shadows due to clouds, and other undesired optical features [31]. The data cube of spectral components, treated as principal components, are to be selected and go through an entropy coder.
  - In the **spatio-temporal processing** block, the image resolution will be enhanced by spatial deconvolution of overlapping images, as indicated in Section IV. Moreover, the spatial features may be segmented and represented in a form that is useful for tracking, classifying and recognizing the features of interest. JPEG2000 algorithm is to be employed for lossless compression of the data that may achieve up to 98 % reduction in size.
  - The processed data may be used for **model update** (i.e. state and parameter estimation) in an onboard oceanographic model that describes the dynamics of the main physical and biological phenomena in the target area. Such phenomena typically include ocean currents, waves and wind as well as transport and production of biological matter of scientific interest.
- The **HYPSO** bus system has functions for attitude control (reaction wheels and magnetic torquers), navigation (GPS), radio communication datalink that can be partially used by the HSI payload, resource/energy/power management, resilience/redundancy/fault-tolerance etc.
- **Ground control** includes overall mission planning and execution, data management, oceanographic model with data assimilation and simulation capabilities, operator interfaces etc. The overall mission management will optimize the use of available resources and assets by providing information and tasks to each one of them.
- **Other assets** include buoys, manned and unmanned aerial/surface/underwater vehicles with payload sensors, traditional satellite data products and meta-ocean services.

A. Data Products

Data products are illustrated in Figure 22. Generally in remote sensing community, the images are defined in levels as can be shown in Table XII[8] below. All exquisite Earth Observation Satellites (EOS) instruments must have Level 1 products. Most are able to downlink Levels 2 and 3 products, but also many have Level 4 products. Level 0 is in general only necessary to characterize the optical performance and degradation. Level 1a and b data is considered useful for remote sensing experts that are more concerned about imagery of Earth. This level may include radiometric correction, onboard calibration and parameters from in-situ validation. Level 0 is recoverable from Level 1a data but not Level 1b and above. Level 2 is most useful for scientists while Level 4 extracts only the necessary information for end-user.

B. Super-resolution

Since overlapping pixels is a key result from the push-broom imaging with constant slew rate, then there are several post-processing deconvolution/super-resolution (SR) algorithms that may be implemented on-board. Basic image

[8]https://science.nasa.gov/earth-science/earth-science-data/data-processing-levels-for-eosdis-data-products/

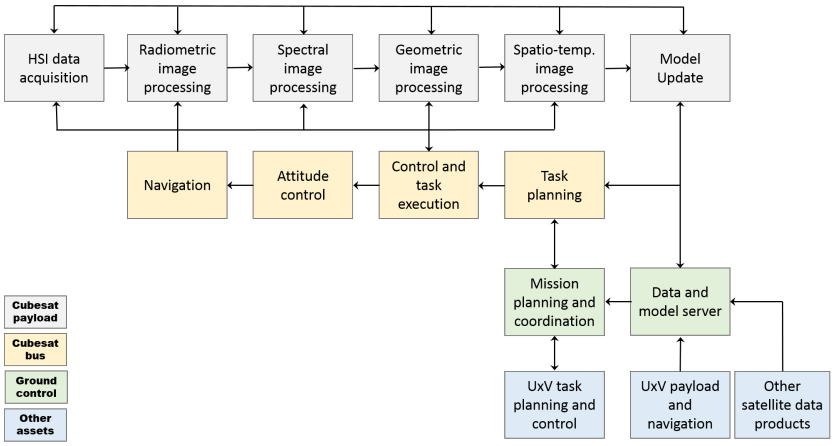

Fig. 21. High-level processing and control architecture for HYPSO

TABLE XII
DATA PROCESSING LEVELS

Data Type	Description
Level 0	Reconstructed, unprocessed instrument and payload data at full resolution, with any and all communications artifacts (e.g., synchronization frames, communications headers, duplicate data) removed. (In most cases, the EOS Data and Operations System (EDOS) provides these data to the data centers as production data sets for processing by the Science Data Processing Segment (SDPS) or by a SIPS to produce higher-level products.)
Level 1a	Reconstructed, unprocessed instrument data at full resolution, time-referenced, and annotated with ancillary information, including radiometric and geometric calibration coefficients and georeferencing parameters (e.g., platform ephemeris) computed and appended but not applied to Level 0 data.
Level 1b	Level 1A data that have been processed to sensor units (not all instruments have Level 1B source data).
Level 2	Derived geophysical variables at the same resolution and location as Level 1 source data.
Level 3	Variables mapped on uniform space-time grid scales, usually with some completeness and consistency.
Level 4	Model output or results from analyses of lower-level data (e.g., variables derived from multiple measurements).

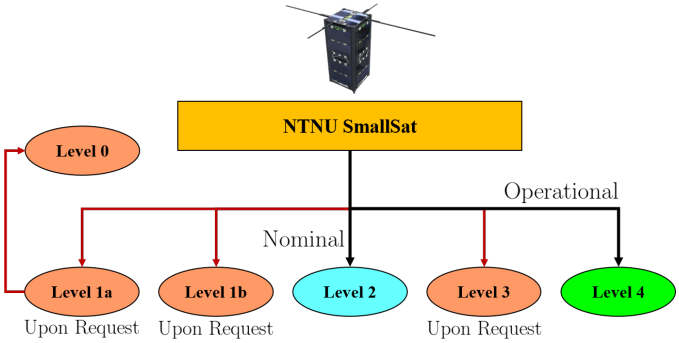

Fig. 22. Data Products delivered by satellite. Level 4 gives operational data that only includes relevant signatures/spectral bands, while Level 2 is useful for science which is not spectrally compressed but has the necessary geometric and spatio-temporal compression. Other formats may be requested by updating the processing levels in a database to be uplinked.

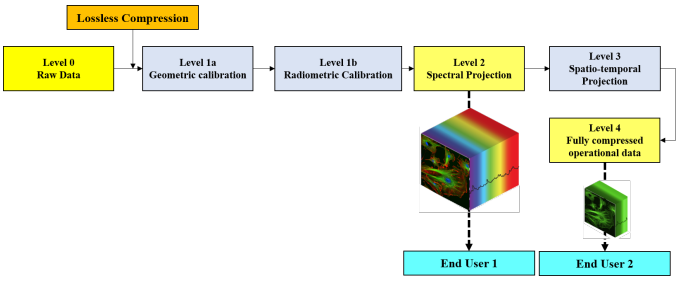

Fig. 23. Data processing products pipeline.

registration for super-resolution is shown in Observing with multiple low-resolution (LR) images has recently proved to be a promising approach to obtain SR image or sequence. This way offers potential lower cost. S. C. Park, M. K. Park and M. G. Kang provide a comprehensive summary of performing SR Image reconstruction through various SR methods [32]. The basis for increasing spatial resolution in SR techniques is the availability of multiple LR images captured from the same scene. The LR images are subsampled or aliased and shifted with subpixel precision. With different subpixel shifts and aliasing present, the image cannot be obtained from the others. However this difference can be utilized for SR reconstruction to achieve better resolution. Relative scene motions must be present from frame to frame via multiple scenes or video sequences. This may be achieved by one camera with several captures or from multiple cameras located in different positions. Motions can be controlled or uncontrolled (i.e. by 'accident').

In the process of recording a digital image, here is a natural loss of spatial resolution caused by the optical distortions such as being out of focus, having diffraction limit, motion

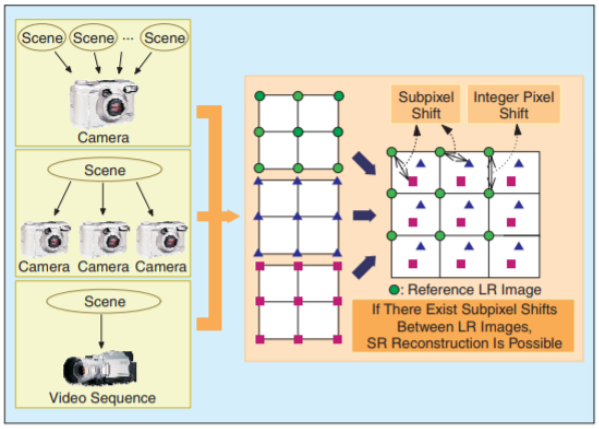

Fig. 24. SR reconstruction. Credit: [32].

blur due to limited shutter speed, noise that occurs within the sensor or during transmission, and insufficient sensor density. In short, SR images are to be reconstructed from degraded and aliased LR images. Therefore SR reconstruction can be considered as a second-generation problem of image restoration. Image interpolation is a method also to be considered in SR reconstruction, that is reconstructing image components that are lost or degraded in the LR sampling process. However high-frequency components cannot be recovered, thus providing an argument for image interpolation not to be considered as a SR reconstruction method.

1) Low-resolution image acquisition process: Formulation of an observation model is necessary to fully understand the analysis of SR image reconstruction. Consider the desired HR image of size $L_1N_1 \times L_2N_2$ written as the vector $\mathbf{x} = [x_1, x_2, \ldots, x_N]^T$, where $N = L_1N_1 \times L_2N_2$. $\mathbf{x}$ is considered to be an ideal undegraded image sampled at or above the Nyquist rate from a bandlimited continous scene (i.e. twice the bandwidth). $L_i, i \in \{1, 2\}$ are the downsampling factors in the observation model for the horizontal and vertical directions. Thus each observed LR image is of size $N_1 \times N_2$. The kth LR image is denoted as $\mathbf{y_k} = [y_{k,1}, y_{k,2}, \ldots, y_{k,M}]^T, k \in \{1, 2, \ldots, p\}$ and $M = N_1 \times N_2$. $\mathbf{x}$ is treated as constant during the acquistion of multiple LR images, except for the motion and degradation allowed by the model. The observation model can then be written as,

$$\mathbf{y_k} = \mathbf{DB_kM_kx} + \mathbf{n_k} \tag{13}$$

where $\mathbf{M_k} \in \mathbb{C}^{L_1N1L_2N_2 \times L_1N_1L_2N_2}$ is a warp matrix and $\mathbf{B_k} \in \mathbb{C}^{L_1N1L_2N_2 \times L_1N_1L_2N_2}$ is a blur matrix, $\mathbf{D} \in \mathbb{C}^{(N1N_2)^2 \times L_1N_1L_2N_2}$ is a subsampling matrix and $\mathbf{n_k}$ represents a ordered noise vector. More about the properties of the matrices can be found in Park et al [32].

Most of the SR image reconstruction methods proposed in the literature consist of registration, interpolation and restoration. These methods can be implemented separately or simultaneously. The following sections will provide summaries of deterministic and stochastic regularization approaches.

2) Nonuniform Interpolation Approach: This technique for SR reconstruction consists of estimation of relative motion (i.e. registration), nonuniform interpolation to produce an improved resolution image and deblurring process. The SR image is obtained from nonuniform interpolation. Deconvolution is employed on the restoration process. Komatsu et al. presented a scheme to acquire an improved resolution image by applying the Landweber algorithm from multiple images taken simultaneously with multiple cameras [33], [34]. They employ block-matching techniques to measure relative shifts. Limitations exist on same aperture of cameras. Different apertures are proposed in this method [35]. Hardie et al. developed a technique for infrared image registration and SR reconstruction by employing registration algorithm for estimating shifts between the acquired frames and presented a weighted nearest neighbor interpolation approach. Wiener filter is finally applied to reduce the effects of blurring and noise caused by the system [36]. Nguyen and Milanfar proposed an efficient wavelet-based SR reconstruction algorithm [37]. The advantage of nonuniform interpolation is that it takes low computational load and makes real-time applications possible.

3) Frequency Domain Approach: This approach utilizes aliasing existing in each LR image to reconstruct a SR image. Three principles govern the frequency domain approach: shifting property of Fourier transform, aliasing relationship between the continuous Fourier transform (CFT) of and original SR image and discrete Fourier transform (DFT) of observed LR images, and finally the assumption that an original SR image is bandlimited. Some methods employ discrete cosine transform (DCT) instead of DFT in order to reduce memory requirements and computational costs. Ill-posedness may be handled by multichannel adaptive regularization parameters [32].

4) Regularized SR Reconstruction Approach: Some of the issues with SR reconstruction approach is due to insufficient number of LR images and ill-conditioned blur operators. Regularization stabilized the inversion of ill-posed problem. Deterministic constrained least squares and stochastic maximum a posteriori SR image reconstruction methods. The deterministic approach is based on using lagrangian multipliers in a minimization problem. This applies well for both large and small number of LR images and will be penalized by the lagrange multiplier accordingly. The stochastic approach is typically of the Bayesian type for a priori sampling and models a priori knowledge to the solution. Some stochastic methods incorporate maximum likelihood (ML) estimation both with a priori and no prior terms. Maximum a posteriori (MAP) is usually preferred over ML due to ill-posed inverse problem. Cheeseman et al. applied the Bayesian estimation with a Gaussian prior model to the problem of integrating multiple satellite images observed by the Viking orbiter [38].

5) Projection onto Convex Sets Approach: This is an iterative approach that incorporates prior knowledge about the solution into the reconstruction process. The SR image is estimated simultaneously through restoration and interpolation. The solution is restricted to be a member of a closed convex set C_t that are defined as a set of vectors which satisfy a particular property. If the constraint sets have a nonempty

intersection then a solution that belongs to the intersection set $C_s = \cap_{t=1}^{m} C_t$, which is also a convex set, can be found by alternating projections onto these convex sets.

6) ML-POCS Hybrid Reconstruction Approach: This approach finds SR estimates by minimizing the ML (or MAP) cost functional while constraining the solution within certain sets. Stochastic approaches and POCS approach may be combined (hybrid).

7) Bayesian Methods for Image SR: L. C. Pickup et al. discuss a novel method of Bayesian image SR in which marginalization is carried out over geometric and photometric registration and image pointspread function [39]. This method allows for more realistic image prior distributions and reduces the integral dimension, easing computational efforts. This is considered here to be an improvement to the more common Bayesian SR approaches that marginalize over the high-resolution image (which needs access to prior unfavourable image). A scheme is developed to deal with this problem by performing Bayesian marginalization over the uncertainty in the set of estimated imaging parameters, leading to an iterative algorithm to estimate a high-resolution image. Improvement to the maximum a posteriori SR estimate can be done by updating LR image registration through SR image estimate. More recently MAP can be used to learn more general geometric and photometric registrations, the SR image and the values for the prior's parameters simultaneously. Tipping and Bishop's *Bayesian Image Super-Resolution* work uses a ML point estimate of the registration parameters and the camera imaging blur, found by integrating the high-resolution image out of the registration problem and optimizing the marginal probability of the observed low-resolution images directly [40]. The accuracy of recovered registration is improved compared to the MAP approach, however, it has limitations of being restricted to use a Gaussian image prior in order for the marginalization to remain tractable and it is computationally expensive. Pickup et al. proposes a better method with smaller matrix sizes thus easing the computations. Constrained optimization methods are used to compute the SR image. The results show that the method is capable of handling the errors and uncertainty introduced in real practical systems and is not mathematically confined to translation-only motion.

8) Robust Estimation and Image Combining: GCOMBINE in the STSDAS package for combining images is described in [41]. With a stack of input images the bad pixels can be identified by comparing the deviation of a pixel from th mean with a user-specified treshold times the clipping sigma. A variety of weighting schemes and means for storing noise characteristics are discussed. Large flux of cosmic ray events are common in space-based CCD cameras. The problem here is to identify and remove such events. Several functionalities of the package are used. After a mean is computed, one computes a deviation of the pixel from the mean and then compare it with a 'clipping sigma'. This way pixels may be rejected. The clipping sigma can only be obtained with either the CCD noise model or the input error map.

9) Restoration of interferometric images. III. Efficient Richardson-Lucy methods for LINC-NIRVANA data reduction: B. Anconelli et al. discuss the methods and software for the restoration of images provided by Fizeau interferometers such as the German-Italian beam combiner LINC-NIRVANA (LN) for the Large Binocular Telescope (LBT) [42]. Multiple images of the same target are provided corresponding to different orientations of the baseline. LN will require multiple-image deconvolution methods in order to produce a unique high-resolution image. Two methods for astronomy image taking are required: the less accurate rapid overview *the quick look method* and *ad hoc method* which is designed for a particular object of interest and is as accurate as possible. Here Richardson-Lucy methods are used as maximization of likelihood function in the case of Poisson noise. The paper also investigates fusion of multiple images into a single one, so that single-image deconvolution methods can be used more efficiently rather than for the multiple-image ones.

C. Other SR Reconstruction approaches

The following are also common approaches for SR Reconstruction:

- Iterative Back-Projection
- Adaptive Filtering
- Motionless SR Reconstruction

VI. Attitude Determination & Control

To achieve the mission success criteria, the ADCS is generally assumed here to include all subsystems necessary for precise pointing and slewing. It does not include 3-axis thrusters, but may be evaluated for a future mission. Two segments of ADCS needs to be worked on: a) attitude & orbit estimation; and b) attitude control. The proposed slewing maneuver for pushbroom imaging is a novel theory-to-practice research field, hence rigorous and novel research is expected in this domain.

A. Mathematical Model

1) Kinematics: Given the quaternion vector expressed in the body frame relative to the inertial frame

$$\mathbf{q}_{ib} \triangleq \begin{bmatrix} \eta_{ib} \\ \boldsymbol{\epsilon}_{ib} \end{bmatrix} \tag{14}$$

where $\boldsymbol{\epsilon}_{ib}$ is defined as

$$\boldsymbol{\epsilon}_{ib} \triangleq \begin{bmatrix} \epsilon_x \\ \epsilon_y \\ \epsilon_z \end{bmatrix} \tag{15}$$

The kinematic differential equations may be written in compact form as

$$\dot{\mathbf{q}}_{ib} = \frac{1}{2} \begin{bmatrix} -\boldsymbol{\epsilon}_{ib}^T \\ \eta_{ib}\mathbf{I}_{3\times 3} + \mathbf{S}\left(\boldsymbol{\epsilon}_{ib}\right) \end{bmatrix} \boldsymbol{\omega}_{ib}^b \tag{16}$$

where $\boldsymbol{\omega}_{ib}^b$ is the angular velocity of the body relative to an inertial frame. $\mathbf{S}(\boldsymbol{\epsilon})$ denotes a skew-symmetric matrix operator, given by

$$\mathbf{S}(\boldsymbol{\epsilon}) = -\mathbf{S}(\boldsymbol{\epsilon})^T = \boldsymbol{\epsilon}^{\times} \triangleq \begin{bmatrix} 0 & -\epsilon_z & \epsilon_y \\ \epsilon_z & 0 & -\epsilon_x \\ -\epsilon_y & \epsilon_x & 0 \end{bmatrix} \tag{17}$$

2) Dynamic Model: The dynamical model for a rigid body actuated by means of external moments and subject to external disturbance moments is given by Eulers momentum equation

$$\mathbf{J}_b \dot{\boldsymbol{\omega}}_{ib}^b = \mathbf{S}\left(\mathbf{J}_b \boldsymbol{\omega}_{ib}^b\right) \boldsymbol{\omega}_{ib}^b + \boldsymbol{\tau}_a^b + \boldsymbol{\tau}_d^b \tag{18}$$

where $\boldsymbol{\omega}_{ib}^b$ is the angular velocity of the body relative to an inertial frame, $\mathbf{J}_b$ is the body inertia matrix, $\boldsymbol{\tau}_a^b$ is the control input and $\boldsymbol{\tau}_d^b$ disturbance moments.

A mathematical model may also be expressed for an internally actuated vehicle. The vehicle consists of an assumed rigid structure, with electronic devices, sensors, etc., and for example four reaction wheels which are spinning about a fixed axis of inertial symmetry, such that the total moment of inertia may be assumed constant in the body frame. Such a mechanical device, consisting of a rigid body combined with several spinning rotors or wheels, is commonly referred to as a gyrostat [ref]. The expression for total angular momentum and axial momentum of the wheels in body frame $\mathcal{F}_b$ may be written as

$$\mathbf{h}^b = \mathbf{J}_b \boldsymbol{\omega}_{ib}^b + \mathbf{A}\mathbf{I}_s \boldsymbol{\omega}_s \tag{19a}$$

$$\mathbf{h}_a = \mathbf{I}_s \mathbf{A}^T \boldsymbol{\omega}_{ib}^b + \mathbf{I}_s \boldsymbol{\omega}_s \tag{19b}$$

where $\mathbf{A} \in \mathbb{R}^{3\times m}$ is a matrix of wheel axis body coordinates, $\mathbf{I}_s \in \mathbb{R}^{m\times m}$ a diagonal matrix of wheel inertias, $\boldsymbol{\omega}_s \in \mathbb{R}^m$ a vector of wheel velocities. Writing in coordinate form in $\mathcal{F}_b$, we obtain

$$\dot{\mathbf{h}}^b + \mathbf{S}\left(\boldsymbol{\omega}_{ib}^b\right) \mathbf{h}^b + \mathbf{S}\left(\mathbf{c}^b\right) \dot{\mathbf{v}}^b = \boldsymbol{\tau}_e^b \tag{20}$$

where $\boldsymbol{\tau}_e^b$ are external torques expressed in body coordinates. Assuming that the origo coincides with the center of mass such that $\mathbf{c}^b \equiv 0$, then we obtain

$$\dot{\mathbf{h}}^b = \mathbf{S}\left(\mathbf{h}^b\right) \bar{\mathbf{J}}^{-1} \left(\mathbf{h}^b - \mathbf{A}\mathbf{h}^a\right) + \boldsymbol{\tau}_e^b \tag{21a}$$

$$\dot{\mathbf{h}}_a = \boldsymbol{\tau}_a \tag{21b}$$

where $\bar{\mathbf{J}} \in \mathbb{R}^{3\times 3}$ is an inertia-like matrix defined as

$$\bar{\mathbf{J}} \triangleq \mathbf{J} - \mathbf{A}\mathbf{I}_s\mathbf{A}^T \tag{22}$$

Thus the dynamical model for an internally actuated satellite may be expressed as

$$\mathbf{J}_b \dot{\boldsymbol{\omega}}_{ib}^b = \mathbf{S}\left(\mathbf{J}_b \boldsymbol{\omega}_{ib}^b\right) \boldsymbol{\omega}_{ib}^b + \mathbf{S}\left(\mathbf{A}\mathbf{I}_s \boldsymbol{\omega}_s\right) \boldsymbol{\omega}_{ib}^b + \mathbf{A}\boldsymbol{\tau}_a^b + \boldsymbol{\tau}_e^b \tag{23a}$$

$$\mathbf{I}_s \dot{\boldsymbol{\omega}}_s = \boldsymbol{\tau}_a^b - \mathbf{I}_s \mathbf{A} \dot{\boldsymbol{\omega}}_{ib}^b \tag{23b}$$

3) External Forces and Moments: External forces and torques affect the satellite while orbiting Earth, both environmental and actuator-generated.

The gravity gradient torque in coordinate vectors expressed in the body system is given as [ref]

$$\boldsymbol{\tau}_g = 3\omega_o^2 (z_{o3}^b)^{\times} \mathbf{I} z_{o3}^b \tag{24}$$

where $\omega_o^2 = \frac{\mu}{R_c^3}$ (R_c^3 and μ are distance between the mass centers of two bodies and gravitational constant of the primary celestial body, $\mathbf{I}$ is the inertia dyadic and the nadir pointing vector in body coordinates is

$$z_{o3}^b = \mathbf{R}_o^b = \mathbf{R}_o^b \begin{bmatrix} 0 \\ 0 \\ 1 \end{bmatrix} \tag{25}$$

The aerodynamical torque on the satellite results from particles in the atmosphere colliding with a non-symmetric cross section. The effects are significant at lower altitudes in LEO. In the worst-case this torque is given by

$$\boldsymbol{\tau}_{ad} = F_{ad}(c_{pa} - c_g) \tag{26}$$

where $F_{ad} = 0.5\rho C_d A V^2$ and ρ is the atmospheric density, C_d is the drag coefficient, A is the surface area, V is the spacecraft velocity, c_{pa} is the aerodynamic center of pressure and c_g is the center of gravity. A controlled magnetic moment may be created by generating a torque given by

$$\boldsymbol{\tau}_m = \mathbf{m} \times \mathbf{B}(t) \tag{27}$$

where $\mathbf{m}$ is the generated magnetic moment and $\mathbf{B}(t)$ is the local magnetic field.

Solar radiation pressure may be expressed as

$$\boldsymbol{\tau}_{sp} = F_{sp}(c_{sp} - c_g) \tag{28}$$

where $\frac{F_s}{c} A_s (1 + q) \cos i$, F_s is the solar constant $1.367\, W/m^2$, c is the speed of light, A_s is the surface area, q is the reflectance factor and i is the angle of incidence of the Sun and c_{sp} is the center of solar pressure.

The total torque due to a reaction wheel assembly is given by

$$\boldsymbol{\tau}_a^b = \mathbf{A}\boldsymbol{\tau}_a \tag{29}$$

where $\boldsymbol{\tau}_a$ is a vector of wheel torques and $\mathbf{A}$ is given by

$$\mathbf{A} = \begin{bmatrix} \sqrt{\frac{1}{3}} & \sqrt{\frac{1}{3}} & -\sqrt{\frac{1}{3}} & -\sqrt{\frac{1}{3}} \\ \sqrt{\frac{2}{3}} & -\sqrt{\frac{2}{3}} & 0 & 0 \\ 0 & 0 & -\sqrt{\frac{2}{3}} & \sqrt{\frac{2}{3}} \end{bmatrix} \tag{30}$$

B. Attitude & Orbit Determination

TBD

C. Slew Maneuver

Based on [7], [10], the key requirements for the HSI are chosen to be:

1) GSD $<$ 40 m/pixel
2) Spectral resolution of 5 nm

In order to make the HSI payload compact (approximately 2.5 U, and less than 600 g), several tradeoffs have been accepted. In particular the design leads to a violation of the 100 meter/pixel GSD in the longitudinal direction when looking Nadir. This is due to two factors:

- The resolution on the ground in the longitudinal direction is 250 m.
- The satellite speed is about 7612.7 m/s, which leads to each pixel being acquired while traveling a distance of about 250 m with a frame rate of 31 fps (frames

per second). Exposure time needs to be high to capture more light.

While an improvement in optical resolution requires a smaller slit width, an improvement in the frame rate requires either a larger slit width, or a larger or more sensitive image sensor. A more sensitive image sensor is currently not easily available without increasing the size and weight of the optics. However, another solution to this problem is enabled by the assumption that the length of the ground track is small compared to the satellite track. As illustrated in Figure 25

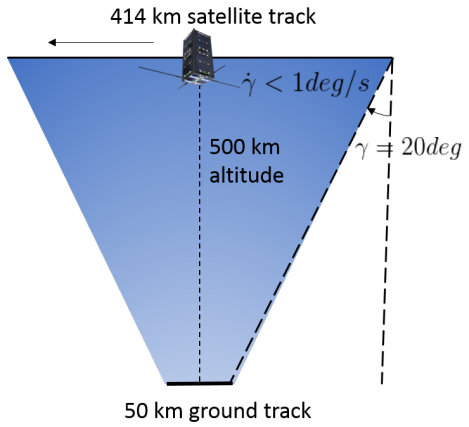

(a) Slewing motion required to point the camera towards a 50 km longitudinal ground track while the satellite is moving in a 414 km in-orbit track.

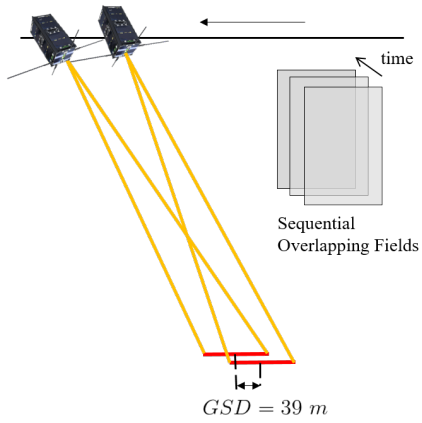

(b) Overlapping pixels aquired by the HSI along the track, achieving $GSD < 40$ m/pixel as a requirement.

Fig. 25. `SmallSat` slewing motion and the constraints.

there are two effects that are achieved by a slewing motion of the satellite:

1) The HSI is slowly scanning the 50 km ground track (assumed to be relatively stationary) over a period of time while the satellite moves 413.7 km in orbit. At an altitude of 500 km, this means that initially the attitude of the satellite will be approximately $\gamma = 20°$ deg relative to Nadir pointing, while at the end of the track the attitude will be approximately $\gamma = -20°$ relative to Nadir. With a satellite moving at $v_{\text{sat}} = 7612.7$ m/s speed, the attitude needs to change approximately $\Delta\gamma = 40°$ during ≈ 54.34 s, i.e. at a rate close to $\dot{\gamma} \approx 0.7361°$/s. The effect of this is that the first two pixels are acquired over 39 m instead of 250 m with exposure time of $\Delta t = 32.8$ ms, contributing significantly to better GSD overall becoming ≤ 39 m during the pass. Equation 3 becomes,
$$\Delta x = \delta x + (v_{\text{sat}} - \dot{\gamma} \cdot h)\Delta t \tag{31}$$
hence the spatial resolution of first frame, after `SmallSat` has slewed during $\Delta t = 32.8$ ms, becomes $\Delta x = 305.1$ m instead of $\Delta x = 500$ m for a Nadir-looking satellite.
2) Since the spatial resolution is $\Delta x = 300$ m and each pixel is acquired over ≤ 39 m, there will be 6 partially overlapping pixels that can be used in a deconvolution filter in order to enhance the image resolution.

Passes are illustrated in Figure 26 showing that overlapping pixels are achieved through slewing. Two actuation segments are necessary as shown in Figure 27 and Figure 28 shows the dynamics of cross-track pointing and slewing.

The slew maneuver, together with nominal attitude control in orbit and pointing to ground station, will be simulated in *AGI STK* to provide a complete spacecraft simulation environment including full rotational dynamics; attitude determination and control; sensor and actuator models; and power and payload modeling.

The target also moves during the HSI observation time slot due to Earth's rotation and needs to be accommodated for in terms of $(x, y, z)_{\text{ECEF}}$ coordinates. This inevitably creates geometric distortions in addition to the issues coming from pointing precision of satellite[9].

D. Spatial Resolution from Slewing

E. Ground Sampling Precision

ADCS requirements are shown in XIII

F. Reaction Wheel Design

The mission requirement of slewing at least $\gamma = 0.7328°/s$, equivalent to $\Delta\gamma = 40°$ during image acquisition to achieve in-track Ground Sampling Distance of $\approx 40\,m$ of $50\,km$ long target area at $500\,km$ altitude. This enables overlapping fields of view to be fused through super-resolution or deconvolution algorithms to enable even higher image resolution than the camera's optical resolution. Given the requirement and constraints, we assume that $1°/s$ is the worst case along 1 axis with respect to Nadir.

The total angular rotation γ produced by a reaction wheel within a given time t_f gives the maximum angular momentum for the satellite [ref]
$$h_{\text{max}} = \frac{2I_{\text{max}}\Delta\gamma}{t_f} \tag{32}$$

[9]Usually $\gamma_{\text{error}} \approx 0.1°(2\sigma)$ is assumed for a 6U CubeSat with all necessary ADCS (Attitude Determination and Control System) components

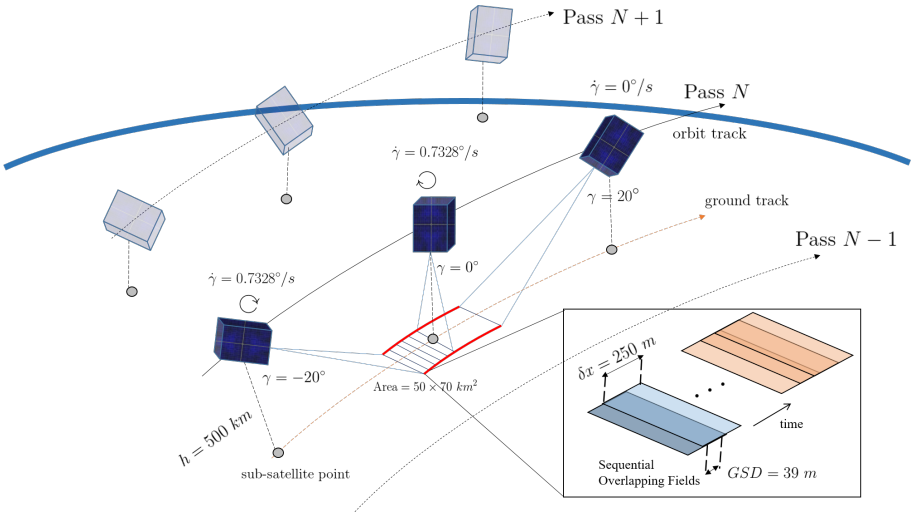

Fig. 26. HYPSO slews above a target area and achieves overlapping pixels. It has three observational passes, where two of them requires HYPSO to point cross-track while slewing.

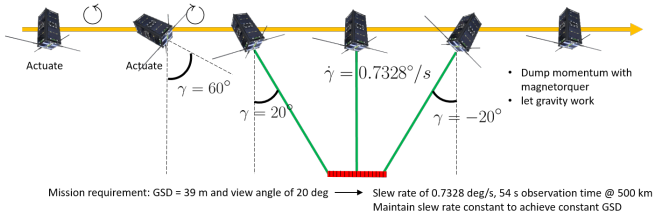

Fig. 27. HYPSO slews in 1 plane ($x-y$ plane wrt Nadir), showing that two actuations are necessary. Momentum is finally dumped by magnetorquers.

TABLE XIII
SLEW MANEUVER CONDITIONS

Performance	**Definition**
Target area (in-track × cross-track)	50 km × 70 km
Altitude (baseline)	500 km
Exposure time	32 ms
Solar zenith angle	$> 15°$
In-track view angle (start; wrt. Nadir)	$+20°$
In-track view angle (end; wrt. Nadir)	$-20°$
In-orbit track distance	413.7 km
Time window for observation	54.3 s
GSD	39 m
Slew rate	$0.7328°$/s
Raw SNR per frame @ 500 nm	≈ 306
Overlapping pixels (in-track)	6
Total SNR per frame @ 500 nm	749.54 (raw SNR $\times\sqrt{\text{frames}}$)
ADCS	**Definition**
Orbit knowledge (GPS)	< 10 m
Pointing accuracy (S/C)	$0.1°$ (2σ)
Drift error (gyroscope)	$1°$/hr
S/C stability	$0.06°$/hr
Settling time	60 s
Mapping error	<100 m
Clock error	<0.1 s
Reaction Wheels	**Definition**
Configuration	Tetrahedral (4 wheels)
Torque	0.2201 mNm
Angular momentum	3.33 mNms
Disk mass (per wheel)	309.8 g
Disk radius (per wheel)	39.15 mm
Motor speed	3700 RPM

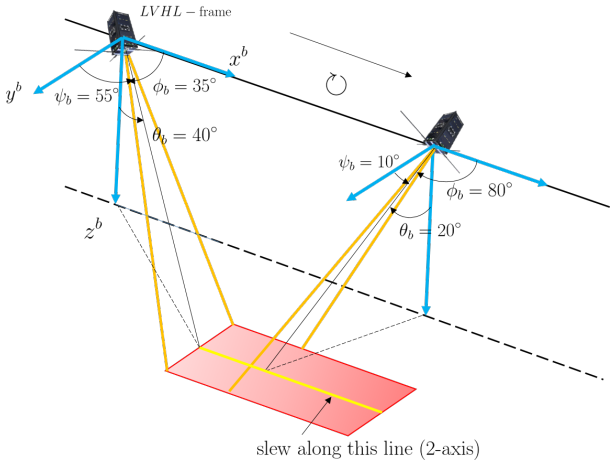

Fig. 28. HYPSO points cross-track to target (actively) while slewing along a line on the ground. This has limitations due to pointing accuracy and substantial movement.

where I_{max} is the greatest inertia of the satellite: for a $6\,kg$ 3U CubeSat this is equivalent to $I_{xx} = 5{\cdot}10^{-2}\ kgm^2$ and for a $12\,kg$ 6U CubeSat this is $I_{xx} = 13 \cdot 10^{-2}\ kgm^2$ [ref]. By selecting a motor with a maximum wheel speed of (average case) $\omega_{\text{max}} = 3700$ rpm, inertia for one wheel can be found as

$$I_{\text{total}} = \frac{h_{\text{max}}}{\omega_{\text{max}}} \tag{33}$$

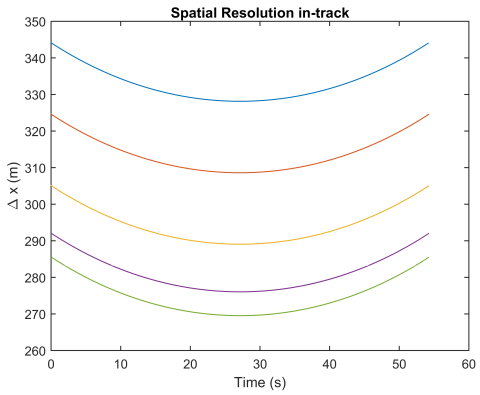

Fig. 29. Spatial Resolution vs. Exposure Time. Blue: Δt =0.0656 s, Red: Δt =0.0492 s, Orange: Δt =0.0328 s, Purple: Δt =0.0219 s, Green: Δt =0.0164 s

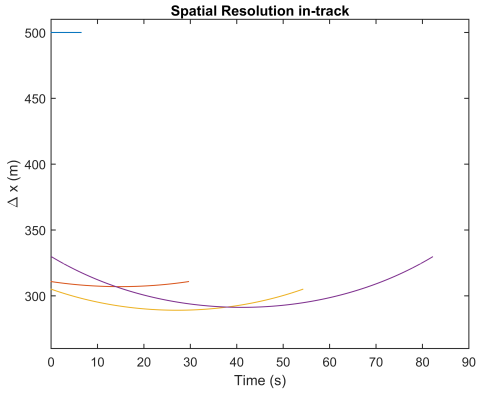

Fig. 30. Spatial resolution versus viewing angle. Blue: γ =0° and $\dot{\gamma}$ =0°/s, Red: γ =10° and $\dot{\gamma}$ =0.6761°/s, Orange: γ =20° and $\dot{\gamma}$ =0.7391°/s, Purple: γ =30° and $\dot{\gamma}$ =0.7277°/s

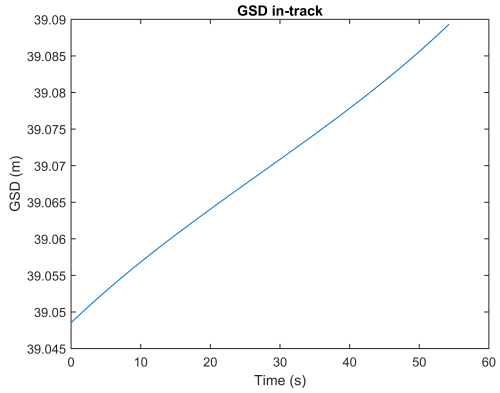

Fig. 31. Ground Sampling Distance vs. Time for Δt =0.0328 s, γ =20° and $\dot{\gamma}$ =0.7391°/s.

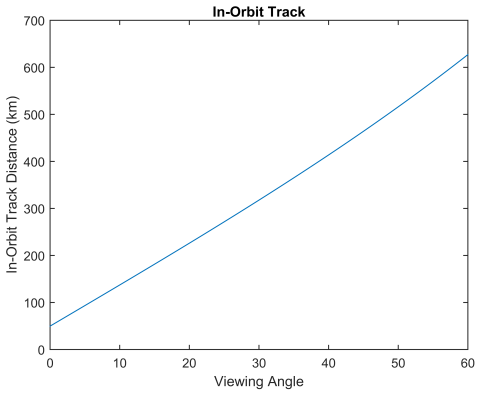

Fig. 32. Viewing Angle effects on In-orbit track distance (km) for observations

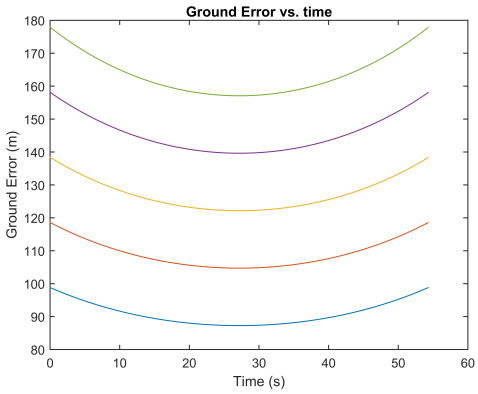

Fig. 33. Ground error during sampling for different pointing precision errors. Blue: $\Delta\gamma$ =0.01°, Red: $\Delta\gamma$ =0.012°, Orange: $\Delta\gamma$ =0.014°, Purple: $\Delta\gamma$ =0.016°, Green: $\Delta\gamma$ =0.018°.

Knowing that for worst case mass and size of reaction wheel when modeled as a disk then

$$I_{\text{total}} = I_{\text{disk}} = \frac{m_{\text{disk}} r_{\text{disk}}^2}{2} \tag{34}$$

where $m_{\text{disk}} = \rho\pi r_{\text{disk}}^2 h_{\text{disk}}$, ρ is the density of iron $7.35 \cdot 10^3\, kg/m^3$, r_{disk} is the radius of the disk and h_{disk} is its height. We also assume that the height of the disk is equal to

$$h_{\text{disk}} = \frac{r_{\text{disk}}}{2} \tag{35}$$

Let's consider a 6U structure with mass $m = 12\, kg$ with $I_{\text{max}} = 13 \cdot 10^{-2}\, kgm^2$. Rearranging the equations above we get that, for a slew rate requirement of $1^\circ/s$ during 54 seconds, that we would require iron material reaction wheel of radius $r_{\text{disk}} \geq 26.1\, mm$ and mass $m_{\text{disk}} \geq 0.2065\, kg$. Figs. 34 and 35 show the systems sizing for different slew rates when mapping the same target area.

G. Initial Simulations

Figure 36 shows the prospected modeling in Simulink for a CubeSat structure using assembly of at least 3 reaction wheels designed in section VI-F. The state vector may be

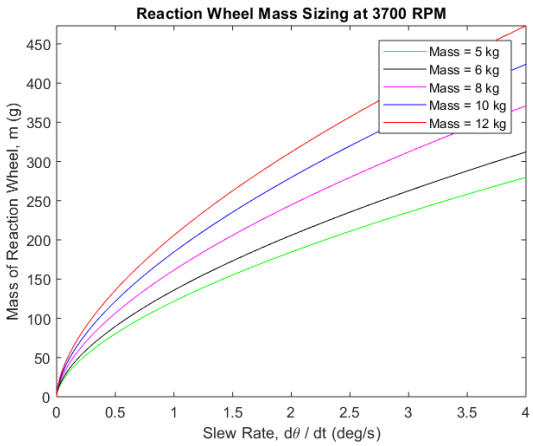

Fig. 34. Reaction Wheel Design Mass vs. Slew Rate

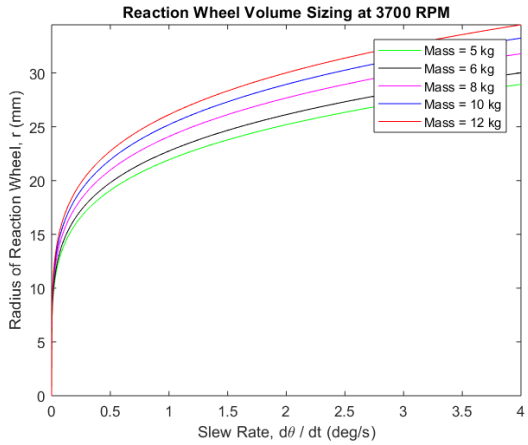

Fig. 35. Reaction Wheel Design Radius vs. Slew Rate

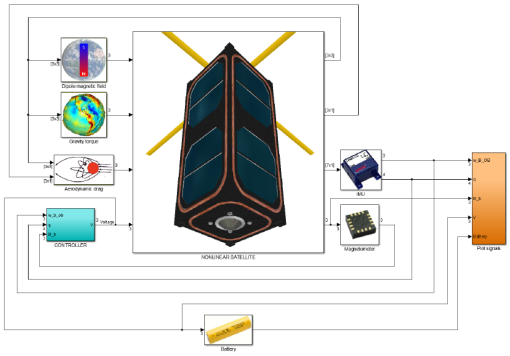

Fig. 36. Nonlinear Simulink Model of Satellite

defined as

$$\mathbf{x} = \begin{bmatrix} \theta \\ \phi \\ \psi \\ \omega_x \\ \omega_y \\ \omega_z \end{bmatrix} \tag{36}$$

Simulations are performed first without perturbations on a Nadir-pointing satellite, with initial conditions set to

$$\mathbf{x} = \begin{bmatrix} 0 \\ 0 \\ 0 \\ 0 \\ 0 \\ 0 \end{bmatrix} \tag{37}$$

and reference is

$$\mathbf{x}_{\text{desired}} = \begin{bmatrix} 11 \\ 2 \\ 0 \\ 0 \\ 0 \\ 0 \end{bmatrix} \tag{38}$$

The temporarily chosen controller is the pointing controller, expressed as

$$u = \tau_a = k_p \cdot \begin{bmatrix} \theta \\ \phi \\ \psi \end{bmatrix} + k_d \cdot \begin{bmatrix} \omega_x \\ \omega_y \\ \omega_z \end{bmatrix} \tag{39}$$

where $k_p = -1.8 \cdot 10^{-4}$ and $k_d = -1.6 \cdot 10^{-3}$. Figs. 37 and 38 show the preliminary results for the pointing controller with selected gains. It is planned that different types of

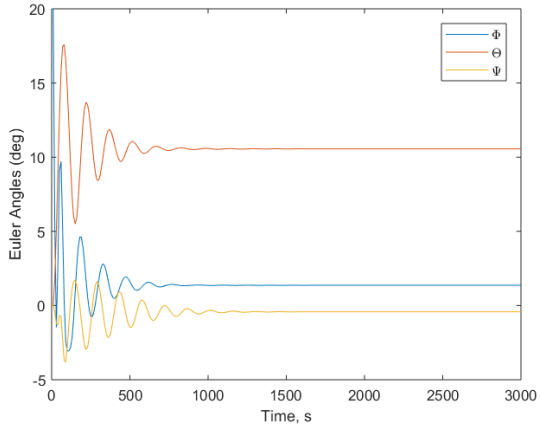

Fig. 37. Euler Angles vs. Time

controllers are to be implemented, as well as observers, including perturbations, and including states of electrical current i_{motor} and power consumption P_{motor}.

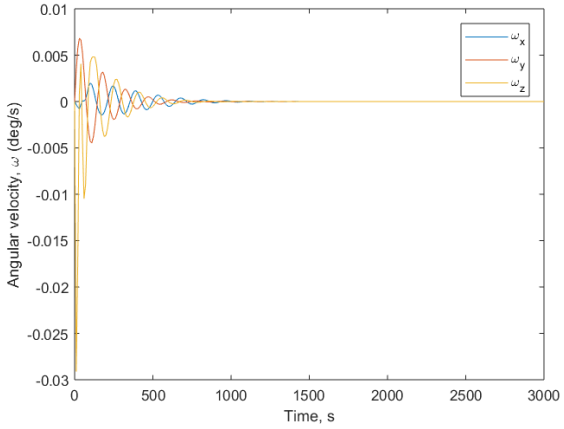

Fig. 38. Angular Velocity vs. Time

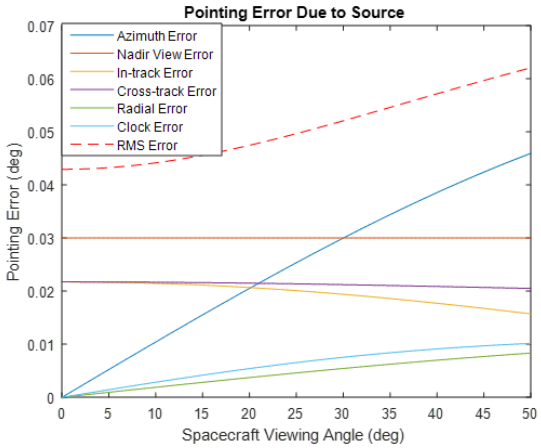

Fig. 40. Pointing errors due to S/C subsystem sources.

H. Errors

There are several orientation errors to consider while imaging a target on ground or pointing actively towards a Ground Station. These include S/C position errors (in-track, cross-track, radial), sensing axis orientation errors (elevation, azimuth), target altitude error, clock errors. Other errors may be mechanical such as e.g. thermal expansions, micro-vibrations and jittering. Pointing errors relate to the imprecision in attitude control and angular motion, while mapping errors concern about the angular motion during the exposure as well as attitude and orbit knowledge (hence most relevant for the slewing maneuver proposed for the HSI mission). The need to understand the sources of errors comes from trade-off analysis between cost vs. performance (size of S/C, how many # of reaction wheels, need for star-tracker, processing power for controllers etc.). Mapping and pointing errors due to fixed sources as a function of S/C viewing angle are shown in Figs. 39 and 40

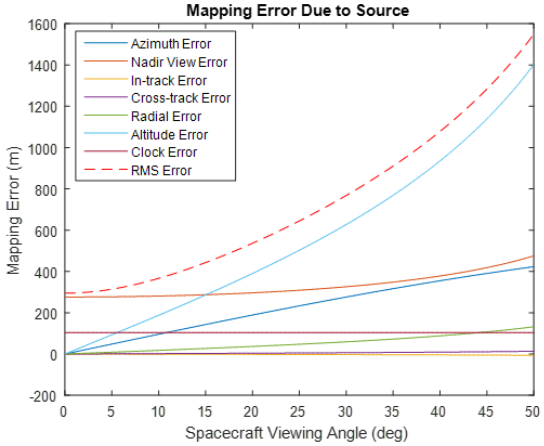

Fig. 39. Mapping errors due to S/C subsystem sources.

VII. Communications

In order to save time during the production/integration phase, it is advised that the payload downlink (and other communication systems) will be procured as a part of the satellite bus. Various suppliers will have different equipment and possibly also different requirements/options/offerings for ground stations. This goes both for the comm systems (TM/TC, payload downlink, ground stations) as well as software for operation.

A. Space segment

As shown, a S-band payload (2 GHz-band) downlink that is capable of 1-2 Mbps will be able to downlink even uncompressed data sets in less than six minutes. Most CubeSat suppliers have such products available. Downlinking at 1-2 Mbps implies pointing of the satellite antenna, at a lower rate (100 kbps) communication should be possible regardless of spacecraft pointing. X-band systems also exist, but are less available. Therefore, and as S-band seems to have enough capacity, X-band is not considered further.

S-band systems also have an output power that can be supported by the CubeSat. In practice, this output power will be quite low (typical 1-10 W). In order to close the link budget, such systems will require an antenna dish of some size (TBC), perhaps with a diameter of 2 to 4 meters mounted on a steerable mast. This must be verified with a link budget calculation when the specifications of the space segment subsystem hardware is known.

During planning and operations, the amount of data generated by the payload must controlled in order to meet the capabilities of the downlink. The communication system might be a bottleneck, so scheduling and operation planning must be done in an efficient manner in order to maximize the amount of data that can be downloaded.

B. Ground Segment

Several architecture options are possible; a) either only own ground station at NTNU (possibly enhanced with ground stations at partner universities and organizations), b) use of commercial stations or c) a combination of a)&b).

a) Local university ground stations: The ground station hardware/software could, depending on cost/schedule/options be based on GS hardware/software from the satellite supplier or be composed by general equipment (or both). The ground station will consist of antennas (dish for S-band, Yagi for VHF/UHF), amplifiers and switches as well as a radio supported by operation software.

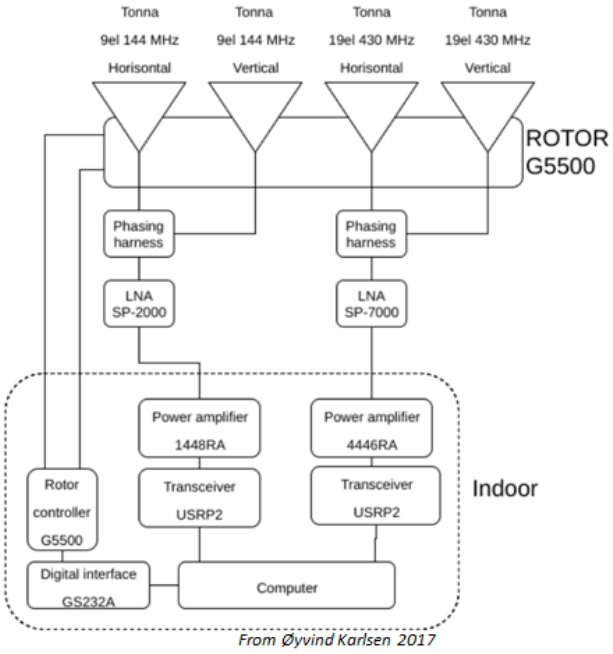

Fig. 41. Schematic of multiband VHF/UHF-station at NTNU

A general schematic of a multi-band ground station is shown in Figure 41 (S-band not currently included). Several academic/open-source designs exists. The design proposed by master student Øyvind Karlsen [43], [44] can be used as a baseline for further study.

Another installation of a versatile ground station based on the use of SDR and GNURadio are being set up at by the university radio club in Trondheim. Partners such as Porto, Vigo and other universities can be potential supporters and help with data acquisition. However, cost and time to build ground stations must be considered.

Setting up own ground stations also has a value by increasing the competence of the organization.

University ground stations should also seek to participate in global ground station network initiatives, such as ESAs revived GENSO-network [10] or the SATNogs-project [11]. The NTNU ground station currently implements and participates in SATNogs.

b) Commercial stations: The use of for example the KSAT Lite should be considered. This might lead to a cost during operations. However, it can be wise to have a backup communication architecture available if the local ground stations cannot be used for some reason.

There are also other companies such as Leaf Space [12] providing ground station services for small satellite missions. Cost and possibilities for all options must be clarified in the next project phase.

c) Combination: In order to quickly downlink data after an image acquisition, multiple ground stations might be desirable. If there is a lack of university partners, the need for a commercial partner can be strong in order to get as much contact time to the satellite as possible. Also, if the satellite during image acquisition moves South to North, a ground station well north of the target should available (e.g. Svalbard).

Another factor to be considered, is the minimum elevation angle needed to close the link budget. Trondheim is far north and will most likely see up to 5 to 6 passes every day (for UHF TM/TC), but S-band downlink might require higher elevation angles in order to close the link budget (TBC) so only 1-3 passes pr. day might be usable.

Stations at Svalbard and Vardø are far north and will therefore see the satellite more times during the day, this alone can be a reason for having to use these stations during mission acquisition operations. Local ground stations can be used for TM/TC and simple operations in order to not incur more costs than necessary.

Further accurate link budget calculations should be performed when more of the system components are known.

C. Ground station and operations software

The satellite bus suppliers will, depending on our needs, deliver software for operating the satellites. When their specification is known, we can derive the need for our own mission planning/scheduling software. Software for interpreting and distributing data will also be required, and should be agnostic wrt. the operations software. Some partner universities have software to consider.

D. Link Budget

The link budget for this mission has been estimated considering an orbit height of 500 km and ground elevation angle $\epsilon = 10°$ for each ground station. This preliminary study has been based on the data provided by GOMspace for the space segment and by KSAT and ISIS for the ground segment. In order to comply with frequency specifications from potential suppliers and partner stations, the downlink frequency carrier will be of about $\approx$ 2250 MHz and the uplink of about $\approx$ 2100 MHz. In addition, to estimate the link budget it has been considered that the transmitter is formed by a power amplifier, some microwave circuits and an antenna; and the receiver is composed by a Low Noise Amplifier (LNA), some microwave circuits and the antenna. Figure 42 shows the representation of the antenna chain for both TX and RX.

Regarding the satellite communication channel, this preliminary propagation losses take into account: free space

[10] http://www.esa.int/Education/Global_Educational_Network_for_Satellite_Operations

[11] https://satnogs.org/

[12] https://leaf.space/leaf-line/

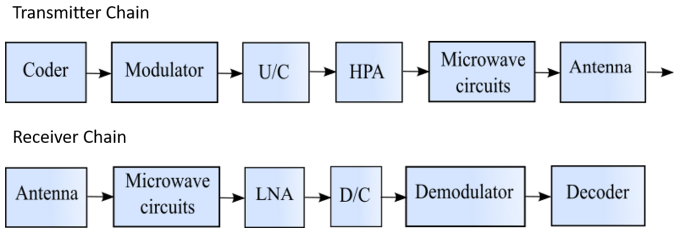

Fig. 42. Block diagram of transmitter and receiving chain

loss, atmospheric gases loss, precipitation loss (considering 0.001 % excess time in Svalbard climatic region) and a rough estimate of pointing, polarization and scintillation losses.

The preliminary link margin for a HYPSO downlinking/uplinking to ground stations, such as KSAT, is shown in Table XIV. Options A, B, C, D are: S-band Downlink (GOMspace + KSAT), S-band Uplink (GOMspace + KSAT), S-band Downlink (GOMspace + ISIS), S-band Uplink (ISIS + GOMspace) respectively.

TABLE XIV
LINK BUDGET

	A	B	C	D
TX				
Power input (W)	0.48	-	26.80	46.99
Antenna gain (dB)	7.90	-	7.90	33.28
Losses (dB)	1.00	-	1.00	1.00
EIRP (dBm)	33.70	74.80	33.70	79.27
Propagation Losses				
Free space loss (dB)	163.88	163.48	163.88	163.88
Atmospheric loss (dB)	4.73	4.73	4.73	4.73
Other losses (dB)	4.00	4.00	4.00	4.00
Tot. propagation loss (dB)	172.6	172.2	172.6	172.60
RX				
Antenna gain (dB)	30.00	7.70	33.28	7.70
Losses (dB)	1.00	1.00	1.00	1.00
Noise figure (dB)	3.77	24.19	8.32	24.19
Bandwidth (MHz)	2	2	2	2
Link Quality				
Carrier power (dBm)	-109.91	-90.70	-106.63	-86.64
Noise power (dBm)	-131.82	-111.40	-127.27	-111.40
Signal to Noise ratio (dB)	21.91	20.69	20.64	24.75
Margin (dB)	14.43	13.20	13.15	17.27

VIII. S/C BUS

HYPSO will be of a 6U standard CubeSat configuration and will include the following subsystems:

- Solar panels (non-deployables)
- Electrical Power System (EPS)
- Remove-Before-Flight (RBF) System
- Kill-switch
- Onboard Computer (OBC)
- Attitude Determination & Control System (ADCS)
  - Magnetorquers (3-axis)
  - 4× reaction wheels
  - 3× sun-sensors
  - Gyroscope/IMU
  - 2× magnetometers
  - Star-tracker
- GPS
- S-band Radio & patch antenna
- UHF Radio & deployable antenna
- Batteries (>54 Wh)

Optional subsystems to include are

- Software-Defined Radio (SDR)
- Cold-gas thrusters (3-axis control)
- Deployable solar panels

Interfacing is prospected to be standard CAN, I^{2}C, SPI and Serial between the subsystems. The mission requirements and payload performance indicate that HYPSO will have the Attitude Determination and Control System to be maximized in performance due to requirement of highest possible pointing precision as well as accurate attitude and orbit knowledge ($< 0.01° \Rightarrow <$ 90m (2σ) error for attitude and $<$ 10m error for orbit position). Figure 43 shows the subsystems required. Table XV shows the estimated mass budget for a 6U SmallSat with the required capabilities.

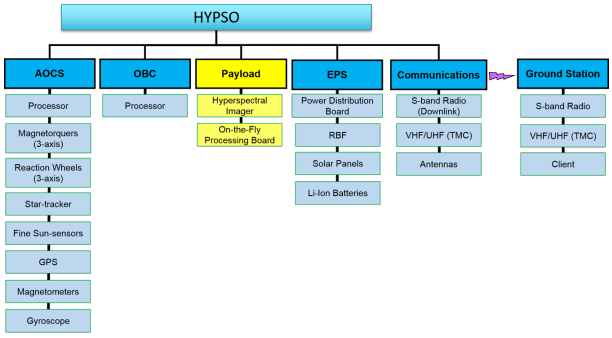

Fig. 43. The subsystems required on both Space and Ground Segments.

TABLE XV
MASS BUDGET FOR A 6U IN GRAMS

Subsystem	Mass, g	Mass, g (+20 %)
HSI	800	960
Structure	1060	1272
Stack rods	123	147.6
Mechanisms	60	72
Wires & cables	200	240
Reaction Wheels	940	1128
Star-tracker	560	672
Fine Sun Sensor	18	21.6
Magnetorquers	156	187.2
ADCS	112	134.4
Antenna S-band	110	132
Antenna UHF/VHF	90	108
Radio S-band	65.3	78.36
Radio UHF/VHF	24.5	29.4
GPS	24	28.8
OBC	94	112.8
EPS	100	120
Batteries	500	600
Solar Panels	758	909.6
SDR	209	250.8
Total	6003.8	7204.56
Total (+20%)		8645.47

IX. Mission Analysis

A. Remote Sensing

In order to bolster the mission design it is necessary to characterize the following

- Identify locations where probability of detection is highest (highest ToA radiance)
- Mapping Chl-a concentration and ToA radiance in the respective locations
- Get ToA radiance and characterize payload sensor
- Identify and create historical database on a daily, monthly and yearly basis with statistics for
  - Cloud cover
  - Chl-a concentrations
  - ToA radiance
- Select targets where `HYPSO` should most likely point to and have it in its database

Figures 44, 45 46 show the Chl-a concentrations and ToA radiances at different dates on the coast of Trondheim, Norway. The data is retrieved from MODIS Aqua with a Multi-spectral instrument (MSI). The radiance reaching the sensor is comparable with respect to the radiance used in Figure 14 used to calculate SNR of HSI V6 in Section IV-C.

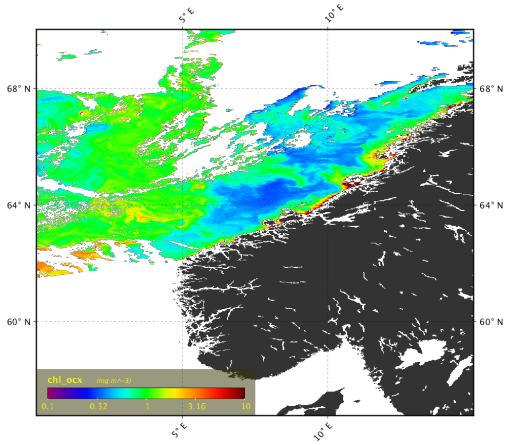

Fig. 44. L2 data showing chl-a concentration outside the coast of Norway taken on 11th of May 2012

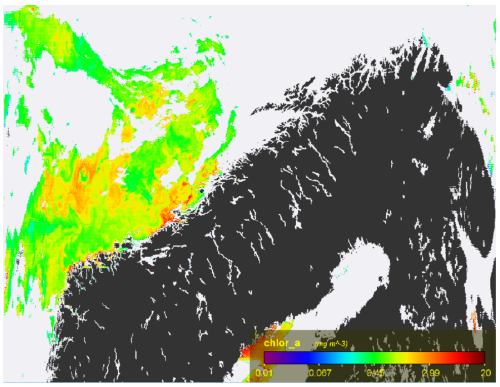

Fig. 45. L2 data showing chl-a concentrations outside the coast of Norway taken on 11th of May 2017

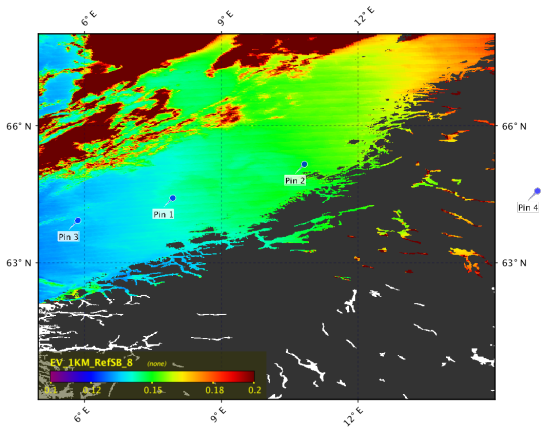

Fig. 46. L1b data showing reflected radiance outside the coast of Norway taken on 11th of May 2012

B. Orbit Analysis

Simulations are run in *STK Analyzer* as an optimization problem to determine maximum of average access duration per day of satellite to target area (Frøya). Simulation period is set to 01/05/2020-17/05/2020 (17 days).
Design variables:

- Ω: RAAN
- i: Inclination
- a: Semi-major axis

Constraints:

- ϵ_{target}: 70° (elevation angle)
- Allowed time: 07:00:00-22:00:00 Local Time
- Maximum range to target: 2000 km

Mission phases and access duration for the satellite sensor are ignored. Unplanned deviations off baseline orbit may be characterized once satellite is in orbit since it is highly dependent on both launch windows (LTAN), delays, deployment of satellite and orbit-insertion. The optimization study determines which launch windows, inclination and altitude the satellite should be inserted to. However the trade study only takes into account the average access duration per day (in seconds), not spatial resolution (an important design variable) determined by optics that e.g. requires lower altitudes.

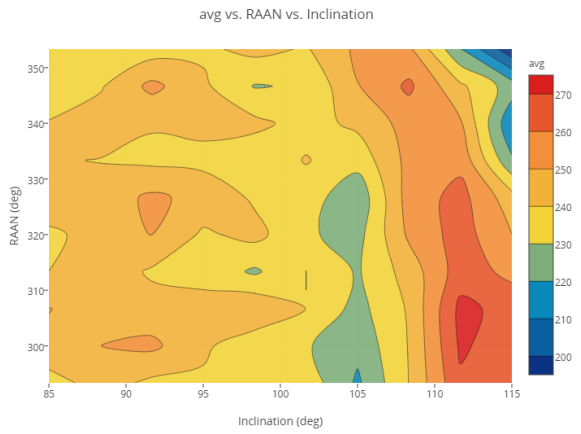

Fig. 47. Contour of Average Access Time to Froya vs. Inclination vs. RAAN

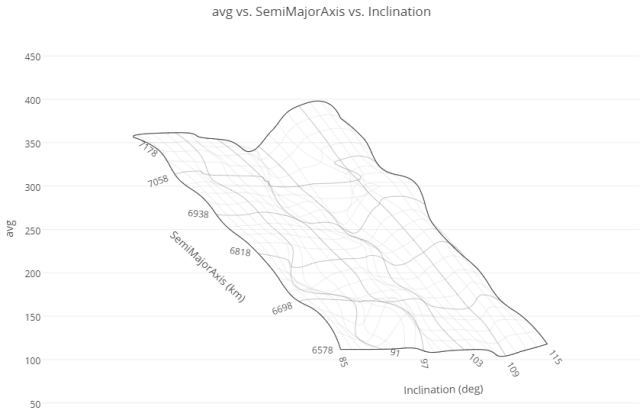

Fig. 48. Average Access Time to Froya vs. Inclination vs. Semi-major axis

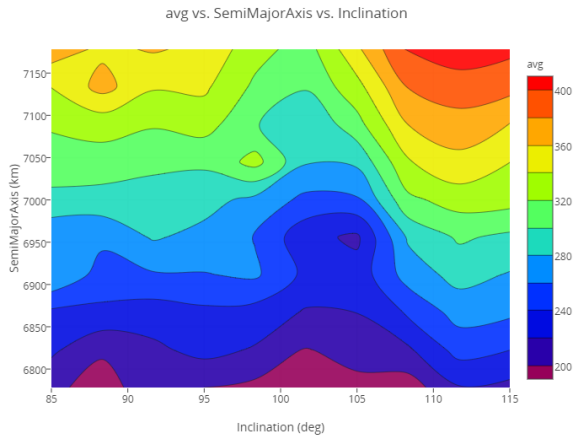

Fig. 49. Contour of Average Access Time to Froya vs. Inclination vs. Semi-major axis

C. Coverage Analysis

TBD

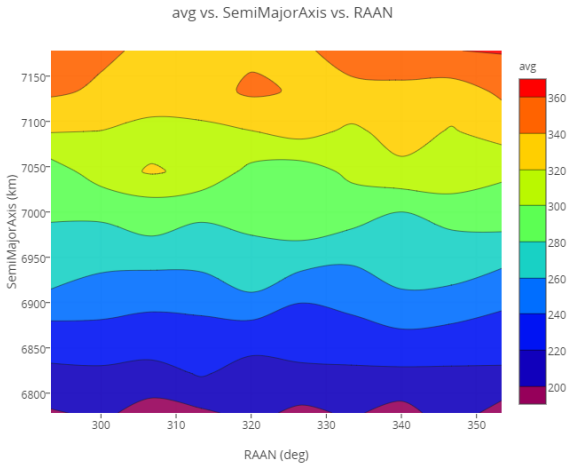

Fig. 50. Contour of Average Access Time to Froya vs. RAAN vs. Semi-major axis

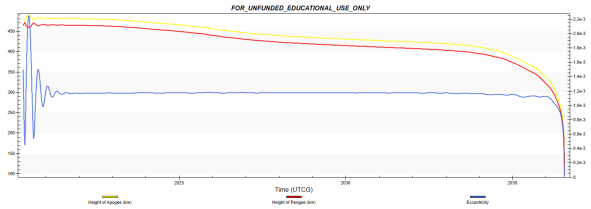

Fig. 51. Lifetime of the satellite in SSO Orbit at 500 km. 7-16 years is expected depending on the altitude when deployed from Launcher.

D. Mission Phases

Mission phases may be summarized in the following Table XVI, assuming 20° viewing angle for HSI observations, 500 km altitude and morning SSO configuration.

TABLE XVI
MISSION PHASES IN ORBIT 1 CONCEPT

Segment	Description	Start (UTC)	Duration (s)
Phase 0	Pre-operations orbit	08:07:00	5400
Phase 1-1	Initialize	09:37:00	15
Phase 1-2	Comms. to Trondheim	09:37:15	125
Phase 1-3	Prepare slewing	09:39:20	115
Phase 1-4	HSI operations	09:41:15	57
Phase 1-5	Data processing	09:42:09	71
Phase 1-6	Point to Svalbard	09:43:25	22
Phase 1-7	Comms. to Svalbard	09:43:45	270
Phase 1-8	Idle (harvest)	09:48:15	605
Phase 1-9	Idle (eclipse)	09:59:20	2207
Phase 1-10	Idle (harvest)	10:36:07	2255
Phase 2	Next operations	11:13:42	5400

E. Data Budget

As discussed in Section V-A, for HYPSO it is considered that Level 0, 1a and 1b may be downloaded upon demand. These may be stored onboard and downlinked in consecutive passes with flexible time constraints. Tables XVII and XVIII show the size and downlink time for all data products with proposed compression method of data and time necessary to downlink for different bands. Option 5 ”Raw B (1735

TABLE XVII

DATA SIZE 1 IMAGE PACKET

Option	Format	Size
1	Raw A (1 frame)	1 × 1200 pixels × 16 bits/pixel × 1 frame = 1.92 Mb
2	Raw A (JPEG2000)	1 × 1200 pixels × 3 bits/pixel × 1 frame = 360 kb
3	Raw B (1735 frames)	1735 × 1200 pixels × 16 bits/pixel = 3.3312 Gb
4	Raw B (JPEG 2000)	1735 × 1200 pixels × 3 bits/pixel = 624.6 Mb
5	Raw C (Raw B deconvoluted)	500 × 1200 pixels × 100 channels × 16 bits/(pixel × channel) = 960 Mb
6	Raw C (JPEG2000)	500 × 1200 pixels × 100 channels × 3 bits/(pixel × channel) = 180 Mb
7	Compressed (spectrally)	500 × 1200 pixels × 21 components × 24 bits/pixel = 302.4 Mb
8	Compressed (spectrally + JPEG2000)	500 × 1200 pixels × 21 components × 3 bits/pixel = 37.8 Mb
9	TT&C & NavData	100 kb

TABLE XVIII

DATA BUDGET, 1 IMAGE PACKET

Format	Size	UHF-band 100 kbps	S-band 1 Mbps	X-band 10 Mbps
Raw A (1 frame) + TT&C	1.92 Mb	20.2 s	2.02 s	0.202 s
Raw A (JPEG2000) + TT&C	360 kb	4.6 s	0.46 s	0.046 s
Raw B (1735 frames) + TT&C	3.3312 Gb	9.26 hrs	55.52 min	5.55 min
Raw B (JPEG2000) + TT&C	624.6 Mb	1.74 hrs	10.41 min	1.04 min
Raw C (Raw B deconvoluted) + TT&C	960 Mb	2.67 hrs	16 min	1.60 s
Raw C (JPEG2000) + TT&C	180 Mb	30.02 min	3 min	18.01 s
Compressed (spectrally) + TT&C	302.4 Mb	50.42 min	5.04 min	30.25 s
Compressed (spectrally + JPEG2000) + TT&C	37.8 Mb	6.32 min	37.9 s	3.79 s
TT&C & NavData	100 kb	1 s	0.1 s	0.01 s

frames)" is defined as raw data (Raw Data A or generally Level 0) that are taken over a 50×70 km target area and has 1735 raw frames that don't undergo deconvolution or super-resolution. Option 6 "Raw C (Raw B deconvoluted)" is defined as an image of 50×70 km target area with frames that have been processed through deconvolution and super-resolution algorithms. Only available data formats with navigational data included that meet the mission requirements are Options 2, 5, 6, 7, 8 i.e. Raw A (1 frame), Raw C (Raw B deconvoluted), Raw C (JPEG2000), Compressed (spectrally), Compressed (spectrally + JPEG2000). The requirements for data processing, based on mission design in section III are summarized in Table XIX. Figures 52 and 53 show the data management for different data products. As shown in Tables XX and XIX it is clear from the access times between HYPSO and Ground Station that L0 and L1 would require several passes to be downlinked through S-band capability. Furthermore, FPGA Programming Logic is relatively large in data size hence would require two passes to be uplinked from Ground to HYPSO .

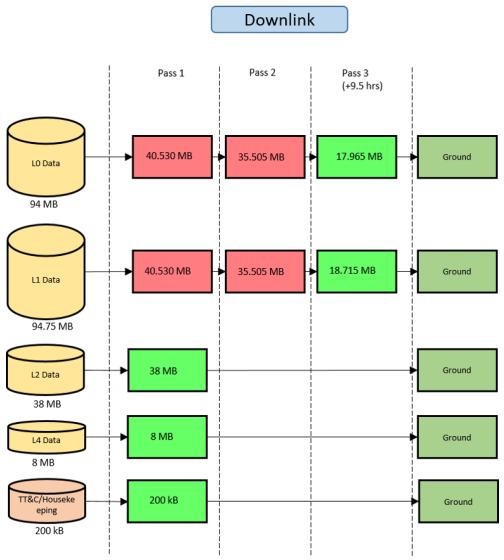

Fig. 52. Data downlink management for various data products.

TABLE XIX

DATA PROCESSING REQUIREMENTS

Parameter	Value
Image resolution (after deconvolution)	500 × 1200 pixels
Principal Components	≤ 21
HSI observation time $[t_{\text{HSI},0}, t_{\text{HSI},f}]$	[0, 54.34] s
Processing time $[t_{\text{process},0}, t_{\text{process},f}]$	[54.34, 115] s
S-band downlink time $[t_{\text{comms},0}, t_{\text{comms},f}]$	[115, 235] s
Nominal data format	Level 4
Science data format	Level 2
Optional data formats	Level 0, 1a, 1b, 3
Format of data to Radio	CAN/RS422

F. Power Budget

The peak power is estimated based on COTS providers in the market[13,14,15] as shown in Table XXI. Main essence will lie in the peak power for the HSI operations in payload capability and antennas/radio for communications, thus in developing the energy budget based on mission operations phases. Software Defined Radio (SDR) for enhanced inter-agent communications is considered, but not baseline for first-flight.

[13]https://gomspace.com

[14]https://www.cubesatshop.com

[15]http://hyperiontechnologies.nl

TABLE XX
MISSION OPERATIONS & CONSTRAINTS

Target area to image	50×70 km^2
Imaging operations duration	1.94 min
1st access time to NTNU	5.129 min
2nd access time to NTNU	7.408 min
3rd access time to NTNU	3.374 min
1st access time to Svalbard	6.755 min
2nd access time to Svalbard	4.743 min
3rd access time to Svalbard (9.5 hrs after 2nd)	5.226 min
Uplink data rate	98 kbps
Downlink data rate	1 Mbps
L0 size	94 MB
L1 size	94.75 MB
L2 size	38 MB
L4 size	8 MB
TT&C size	200 kB
Uplink FPGA logic size	6 MB
Uplink mission plan size	200 kB
Downlink time L0	12.492 min
Downlink time L1	12.64 min
Downlink time L2	5.04 min
Downlink time L4	1.0584 min
Downlink time TT&C	1.6 s
Uplink FPGA logic time	8.16 min
Uplink mission plan time	16.33 s
# passes to downlink L0, L1	3
# passes to downlink L2	1
# passes to downlink L4	1
# passes to downlink TT&C	1
# passes to uplink FPGA logic	2
# passes to uplink mission plan	1

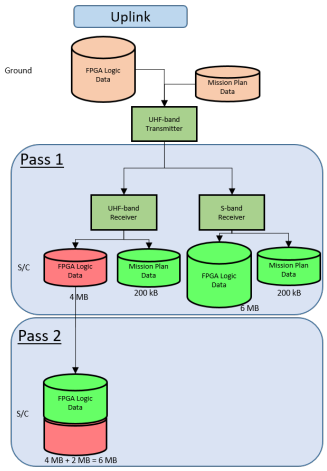

Fig. 53. Data uplink management for various data products.

G. Energy Budget

Given Orbit concept 1 configuration as discussed in section III-D.2 and Table XVI where HYPSO passes Norway from south to north, there are mission phases to identify regarding energy management. Assuming there exists 30 % discharge in the batteries and efficiency of solar power ratings are 30-40 %, the energy budget for the respective mission phases are shown in Table and XXII for a 6U (Battery capacity = 5200 mAh, Max solar power = 12.88 W, Min solar power = 3.86 W), respectively. It is assumed that HYPSO is continuously downlinking data during Phase 7 in order to add flexibility in terms of raw data download

TABLE XXI
POWER CONSUMPTION OF SUBSYSTEMS

Subsystem	Avg., W (+30 %)	Peak, W (+30 %)
HSI	3.9	10.4
Mechanisms	0	0.017
TT&C	0.065	0.13
Reaction Wheels	0.663	3.315
Star-tracker	0.91	1.3
Fine Sun Sensor	0.052	0.052
Magnetorquers	0.78	0.78
ADCS	0.306	1.255
Antenna S-band	0.78	13.91
Antenna UHF/VHF	0.78	13.91
Radio S-band	17.16	18.72
Radio UHF/VHF	5.304	5.304
GPS	1.5015	1.56
OBC	0.221	1.17
EPS	0.0975	0.195
Batteries	0.0052	0.0052

or inadequate quality of communications.

It can be inferred from the energy budgets (fairly conservatively estimated in terms of power supply from solar power and battery capacity), that a 3U size SmallSat would struggle remaining operational for 3 consecutive HSI operations and downlinking together. A 6U adds more flexibility in terms of having enough power to sustain several operations in even one pass, not only once in a pass.

H. Backup Mission

TBD

X. GROUND DISTRIBUTION SYSTEM

A. Architecture

Overview of the Ground Distribution System (GDS) and HYPSO functionality is shown in Figure 54.

B. Planning & Scheduling

Planning & scheduling according to the constraints of mission phases is shown in Figure 55.

XI. SYSTEMS ENGINEERING

A characteristic of small satellites is that they are developed using Components-Off-The-Shelf (COTS), reduced amount of rigorous testing according to traditional space standards, and much lower cost and shorter schedule. However, small satellites, especially in university settings, have a high infant mortality rate [45], and sometimes never end up launching because of funding running out or team members leaving. There has been a concerted effort into making an ISO standard for small satellites, as well as research into improving reliability of the flight products.

The HSI mission will utilize different methods of rapid system engineering to *reduce the time between mission concept definition and launch, by still maintaining acceptably low risk and cost.* This research will start the development of a methodology based on lean and other system engineering principles tailored to a university environment of space engineering. This includes finding tools to support the product

TABLE XXII
ENERGY BUDGET FOR 6U

Mission segment	Duty Cycle (s)	Power in (W)	Power in (Wh)	Power Consumed (Wh)	Start Power (Wh)	End Power (Wh)
Phase 0	5400	12.88	0.02	0.02	53.90	53.90
Phase 1	5	12.88	0.02	0.02	53.90	53.90
Phase 2	125	6.44	0.22	1.15	53.90	52.98
Phase 3	115	3.86	0.12	0.54	52.98	52.56
Phase 4	57	3.86	0.06	0.64	52.56	51.98
Phase 5	71	6.44	0.13	0.40	51.98	51.71
Phase 6	22	6.44	0.04	0.21	51.71	51.54
Phase 7	270	3.86	0.29	3.34	51.54	48.50
Phase 8	605	12.88	2.16	1.29	48.88	49.76
Phase 9	2207	0.00	0.00	5.03	49.76	44.73
Phase 10	2255	12.88	8.07	3.29	44.73	49.51
Phase N+1 (active)	660		0.88	5.90	49.51	44.49
Phase N+1 (idle)	5359		10.23	9.61	44.49	45.12

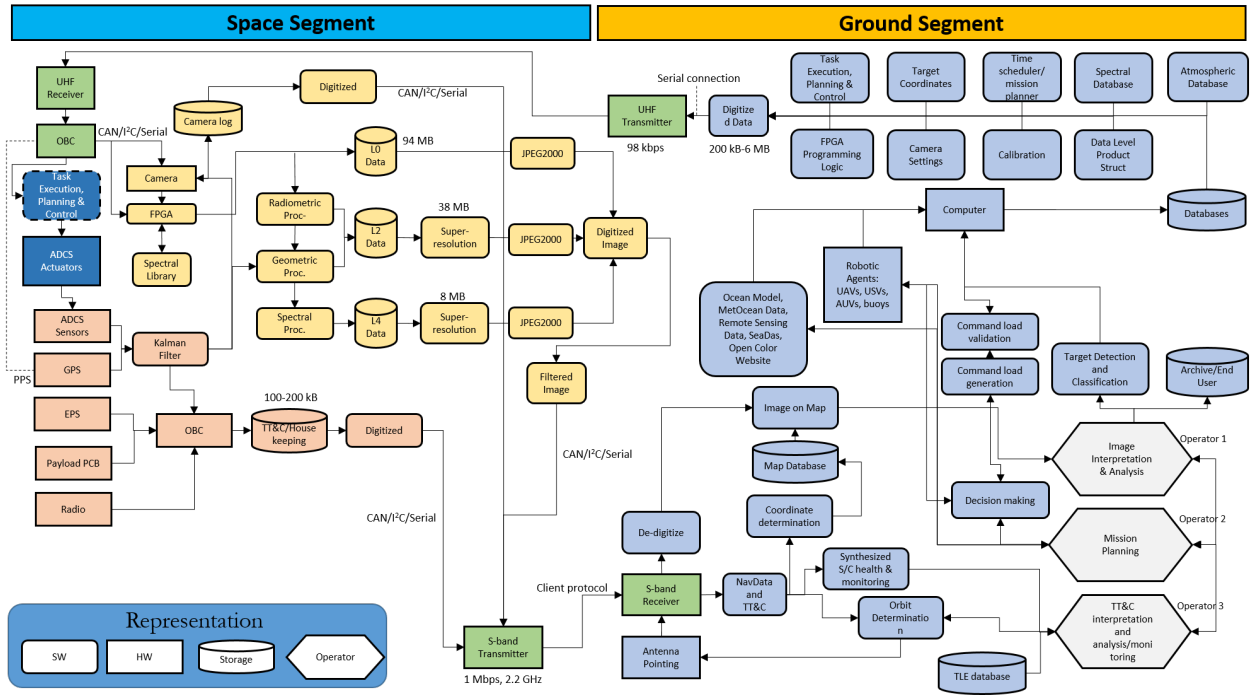

Fig. 54. Overview of the GDS

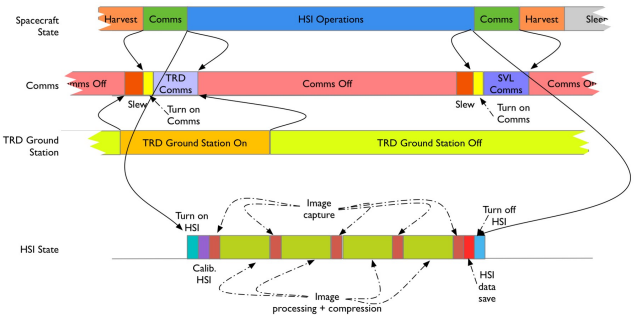

Fig. 55. Planning & Scheduling required based on mission phases described in Table XVI

development that are both cross-platform, preferably open source, and lean.

The two methodologies used in the preliminary system engineering phases are:

- **Model Based System Engineering (MBSE)**: is a methodology where models are in focus for information exchange, instead of traditional document-based exchange. Systems Modeling Language (SysML) has been utilized as modeling language, which is an extension of Unified Modeling Language (UML) to support "'the specification, analysis, design, verification and validation of a broad range of systems"'[46]. By developing the product with SysML, the different building blocks can be connected to requirements, and a requirements traceability matrix can be used for systematic control of verification during testing. Using SysML however, requires some knowledge of UML as well as good tools to be able to use it in an agile manner.
- **Concurrent Engineering (CE)**: is a methodology where engineering is done in parallel, instead of in

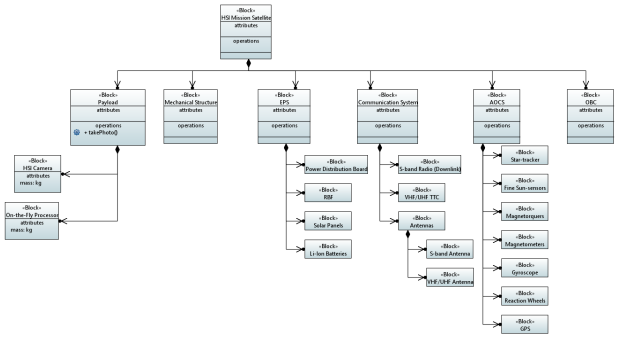

Fig. 56. Product Tree created with SysML 1.4

series (waterfall product development). It requires a multi-platform exchange of models, as well as solutions that enable design to be developed by different people at the same time (such as cloud solutions). It is used by European Space Agency (ESA) at their Concurrent Design Facility, which also offers workshops for students and start-ups in space product development.

A. Product Description

The basic product tree was created using SysML with Oxygen Eclipse Papyrus, see 56.

B. Model Philosophy

The ISO standard 19683 [47] provides the minimum requirements for qualification and testing of small satellites. Based on the fact that most small satellites utilize COTS and employ less strict testing and product assurance routines. There will be two model philosophies for this mission; one for the payload and one for the integrated system.

1) Payload: The payload has not been space-proven previously, and according to the CE philosophy, its subsystems will be developed in parallel. In practice, this means that the algorithms for signal processing, the mechanics, the optics, the electronics and others will all follow separate tracks of development - but with regular testing. For example, the first version of the payload has already been flown on a drone with a non-mission specific camera module to ensure performance of the optics, while the space-specific camera module and electronics were being developed. That way the optics' performance could be tested and improved without having to wait for the camera and electronics.

2) Integrated system: The integrated system consists of the satellite bus purchased from a 3rd party, into which the payload is integrated.

C. Hardware Development Plan

D. Software Development Plan

E. Assembly, Integration, Test (AIT)

F. Interface Description

G. COTS

XII. Conclusions

TBD

XIII. Future Work

TBD

Acknowledgments

This work was supported by the Research Council of Norway, Statoil, DNV GL and Sintef through the Centers of Excellence funding scheme, Grant 223254 - Center for Autonomous Marine Operations and Systems (AMOS) and the Research Council of Norway through the IKTPLUSS programme grant 270959.

This work is also supported by the Norwegian Space Centre contract SAT.01.17.7.

References

[1] J. Bellingham and K. Rajan, "Robotics in Remote and Hostile Environments," *Science*, vol. 318, no. 5853, pp. 1098–1102, 2007.

[2] T. B. Curtin, J. G. Bellingham, J. Catipovic, and D. Webb, "Autonomous oceanographic sampling networks," *Oceanography*, vol. 6, pp. 86 – 94, 1993.

[3] M. Faria, J. Pinto, F. Py, J. Fortuna, H. Dias, R. Martins, F. Leira, T. A. Johansen, J. Sousa, and K. Rajan, "Coordinating uavs and auvs for oceanographic field experiments: Challenges and lessons learned experiments in uav and auv control for coastal oceanography," in *IEEE Int. Conf. Robotics and Automation, Hong Kong*, 2014.

[4] D. A. Jessup, M. A. Miller, J. P. Ryan, H. M. Nevins, H. A. Kerkering, A. Mekebri, D. B. Crane, T. A. Johnson, and R. M. Kudela, "Mass stranding of marine birds caused by a surfactant-producing red tide," *PLOS ONE*, vol. 4, no. 2, pp. 1–8, 02 2009. [Online]. Available: https://doi.org/10.1371/journal.pone.0004550

[5] G. Johnsen, M. A. Moline, L. H. Pettersson, J. Pinckney, D. V. Pozdnayakov, E. S. Egeland, and O. M. Schofield, *Optical monitoring of phytoplankton bloom pigment signatures*. Cambridge University Press, 2011, ch. 14, pp. 538–606.

[6] H. Dierssen, G. B. McManus, A. Chlus, D. Qiu, B.-C. Gao, and S. Lin, "Space station image captures a red tide ciliate bloom at high spectral and spatial resolution," *Proceedings of the National Academy of Sciences*, vol. 112, no. 48, pp. 14 783–14 787, 2015.

[7] K. R. Turpie, S. Ackelson, T. Bell, H. Dierssen, J. Goodman, R. O. Green, L. Guild, E. Hochberg, V. V. Klemas, S. Lavender, C. M. Lee, P. Minnett, T. Moisan, F. Muller-Karger, J. Ortiz, S. Palacios, D. R. Thompson, and R. Zimmerman, "Global observations of coastal and inland aquatic habitats," NASA, Tech. Rep., 2016. [Online]. Available: https://doi.org/10.13140/RG.2.2.15839.66729

[8] A. G. C. Guerra, F. Francisco, J. Villate, F. Agelet, O. Bertolami, and K. Rajan, "On small satellites for oceanography: A survey," *Acta Astronautica*, vol. 127, pp. 404–423, 2016.

[9] M. Guelman and F. Ortenberg, "Small satellite's role in future hyperspectral earth observation missions," *Acta Astronautica*, vol. 64, no. 11, pp. 1252–1263, 2009.

[10] T. D. Dickey and R. R. Bidigare, "Interdisciplinary oceanographic observations: the wave of the future," *Scientia Marina*, vol. 69, pp. 23–42, 2005.

[11] M. S. Garcia-Cascales and M. T. Lamata, "On rank reversal and TOPSIS method," *Mathematical and Computer Modelling*, vol. 56, no. 5–6, pp. 123–132, 2012.

[12] R. W. Saaty, "The analytic hierarchy processwhat it is and how it is used," *Mathematical Modelling*, vol. 9, no. 3–5, pp. 161–176, 1987.

[13] P. Mouroulis, B. V. Gorp, R. O. Green, H. Dierssen, D. W. Wilson, M. Eastwood, J. Boardman, B. Gao, D. Cohen, B. Franklin, F. Loya, S. Lundeen, A. Mazer, I. McCubbin, D. Randall, B. Richardson, J. I. Rodriguez, C. Sarture, E. Urquiza, R. Vargas, V. White, and K. Yee, "The Portable Remote Imaging Spectrometer (PRISM) coastal ocean sensor: design, characteristics and first flight results," *Applied Optics*, vol. 53, no. 7, pp. 1363–1380, 2014.

[14] X. Prieto-Blanco, C. Montero-Orille, B. Couce, and R. de la Fuente, "Analytical design of an Offner imaging spectrometer," *Optics Express*, vol. 14, no. 20, 2006.

[15] Y. Zonga, S. W. Browna, G. Meisterb, R. A. Barnesc, and K. R. Lykke, "Characterization and correction of stray light in optical instruments," *Proc. of SPIE*, vol. 6744, 2007.

TABLE XXIII
MODEL PHILOSOPHY - INTEGRATED SYSTEM

Model Name	**Engineering Bread Board**	**Qualification Model**	**Flight Model**
Purpose	Functional verification	Qualification Tests	Flight
Components Grade	Commercial-off-the-Shelf	Industrial grade / automotive parts	Flight/MIL/industrial grade / automotive parts
Configuration	Same function as in the QM, but not the same structure	Same as flight (except for radiation-sensitive components etc.)	Flight configuration
Test	Functional and interface testing. Preliminary thermal of components	Qualification test	Acceptance tests

[16] M. R. Corson and C. O. Davis, "A New View of Coastal Oceans From the Space Station," *EOS, Transactions, American Geophysical Union*, vol. 92, pp. 161–168, 2011.

[17] D. Blondeau-Patissier, J. F. Gower, A. G. Dekker, S. R. Phinn, and V. E. Brando, "A review of ocean color remote sensing methods and statistical techniques for the detection, mapping and analysis of phytoplankton blooms in coastal and open oceans," *Progress in Oceanography*, vol. 123, pp. 123–144, 2014.

[18] S. Emberton, L. Chittka, A. Cavallaro, and M. Wang, "Sensor Capability and Atmospheric Correction in Ocean Colour Remote Sensing," *Remote Sensing*, vol. 8, 2016.

[19] Z. Lee, S. Shang, G. Lin, J. Chen, and D. Doxaran, "On the modeling of hyperspectral remote-sensing reflectance of high-sediment-load waters in the visible to shortwave-infrared domain," *Applied Optics*, vol. 55, pp. 1738–1750, 2016.

[20] D. A. Siegel, M. Wang, S. Maritorena, and W. Robinson, "Atmospheric Correction of Satellite Ocean Color Imagery: The Black Pixel Assumption," *Applied Optics*, vol. 39, 2000.

[21] W. Moses, A. Gitelson, S. Berdnikov, J. Bowles, V. Povazhnyi, V. Saprygin, E. Wagner, and K. Patterson, "HICO-Based NIRRed Models for Estimating Chlorophyll-a Concentration in Productive Coastal Waters," *IEEE Geoscience and Remote Sensing Letters*, 2013.

[22] R.-R. Li, R. Lucke, D. Korwan, and B.-C. Gao, "A technique for removing second-order light effects from hyperspectral imaging data," *IEEE Trans. Geosci. Remote Sens.*, vol. 50, pp. 824–830, 2012.

[23] F. Sigernes, M. Syrjasuo, R. Storvold, J. Fortuna, M. Grøtte, and T. A. Johansen, "A 3D printed hyperspectral imager," University Center in Svalbard, Tech. Rep., 2017.

[24] C. Hu, L. Feng, Z. Lee, C. O. Davis, A. Mannino, C. R. McClain, and B. A. Franz, "Dynamic range and sensitivity requirements of satellite ocean color sensors: Learning from the past," *Applied Optics*, vol. 51, p. 60456062, 2012.

[25] N. R. Council, "Earth science and applications from space: National imperatives for the next decade and beyond," Washington, DC, USA: The National Academic Press, 2007.

[26] A. Gitelson, B. C. Gao, R.-R. Li, S. Berdnikov, and V. Saprygin, "Estimation of chlorophyll-a concentration in productive turbid waters using a Hyperspectral Imager for the Coastal Oceanthe Azov Sea case study," *Environmental Research Letters*, vol. 6, 2011.

[27] W. D. Philpot, "Atmospheric Effects in Remote Sensing," *IEEE Transactions on Geoscience and Remote Sensing*, vol. 29, no. 3, 1991.

[28] T. T. Wynne, R. P. Stumpf, and T. O. Briggs, "Comparing MODIS and MERIS spectral shapes for cyanobacterial bloom detection," *International Journal of Remote Sensing*, 2013.

[29] M. Soukup, J. Gailas, D. Fantin, A. Jochemsen, C. Aas, P. J. Baeck, L. Benhadj, S. Livens, B. Delauré, M. Menenti, B. G. H. Gorte, S. E. Aria Hosseini, M. Esposito, and C. N. van Dijk, "Hyperscout: Onboard processing of hyperspectral imaging data on a nanosatellite," in *Small Satellites, System and Services Symposium (4S), Valletta, Malta*, 2016.

[30] R. Vitale, A. Zhyrova, J. F. Fortuna, O. E. de Noord, A. Ferrer, and H. Martens, "On-the-fly processing of continuous high-dimensional data streams," *Chemometrics and Intelligent Laboratory Systems*, vol. 161, pp. 118–129, 2017.

[31] J. F. Fortuna and H. Martens, "Multivariate data modelling for de-

[32] S. C. Park, M. K. Park, M. G. Kang, "Super-resolution image reconstruction: a technical overview," *Signal Processing Magazine, IEEE*, vol. 20, no. 3, p. 2136, May 2003.

shadowing of airborne hyperspectral imaging," *J. Spectral Imaging*, vol. 6, 2017.

[33] T. Komatsu, K. Aizawa, T. Igarashi, T. Saito, "Signal-processing based method for acquiring very high resolution image with multiple cameras and its theoretical analysis," *Proc. Inst. Elec. Eng.*, vol. 140, no. 1, pp. 19–25, February 1993.

[34] L. Landweber, "An iteration formula for Fredholm integral equations of the first kind," *Amer. J. Math.*, vol. 73, pp. 615–624, 1951.

[35] T. Komatsu, T. Igarashi, K. Aizawa, T. Saito, "Very high resolution imaging scheme with multiple different-aperture cameras," *Sinal Processing: Image Commun.*, vol. 5, pp. 511–526, December 1993.

[36] M.S. Alam, J.G. Bognar, R.C. Hardie, B.J. Yasuda, "Infrared image registration and high-resolution reconstruction using multiple translationally shifted aliased video frames," *IEEE Trans. Instrum. Meas.*, vol. 49, pp. 915–923, October 2000.

[37] N. Nguyen, P. Milanfar, "An efficient wavelet-based algorithm for image superresolution," *Proc. Int. Conf. Image Processing*, vol. 2, pp. 351–354, 2000.

[38] P. Cheeseman, B. Kanefsky, R. Kraft, J. Stutz, R. Hanson, "Super-resolved surface reconstruction from multiple images," NASA Ames Research Center, Moffett Field, CA, Tech. Rep. FIA-94-12, December 1994.

[39] L. C. Pickup, D. P. Capel, S. J. Roberts, A. Zisserman, "Bayesian methods for image super-resolution," *The Computer Journal*, vol. 52, no. 1, pp. 101–113, 2009.

[40] M. E. Tipping, C. M. Bishop, "Bayesian image super-resolution," in *Advances in Neural Information Processing Systems 15.*, In Becker, S., Thrun, S. and Obermayer, K., Ed., 2003.

[41] C.Y. Zhang, "Robust estimation and image combining," *Astronomical Data Analysis Software and Systems IV*, vol. 77, p. 514, 1995.

[42] B. Anconelli, M. Bertero, P. Boccacci, M. Carbillet, "Restoration of interferometric images. III. Efficient Richardson-Lucy methods for LINC-NIRVANA data reduction," *Astronomy & Astrophysics*, vol. 431, no. 2, p. 747755, 2005.

[43] Ø. Karlsen, "Ground station considerations for the amos satellite programme," mathesis, Norwegian Univesity of Science and Technology (NTNU), 2017. [Online]. Available: https://brage.bibsys.no/xmlui/handle/11250/2462967

[44] A. radioklubb, "Progress report on 1 to 10 GHz parabolic dish project," 2107, internal report.

[45] P. Faure, A. Tanaka, and M. Cho, "Toward lean satellites reliability improvement using horyu-iv project as case study," *Acta Astronautica*, vol. 133, no. Supplement C, pp. 33 – 49, 2017. [Online]. Available: http://www.sciencedirect.com/science/article/pii/S009457651630724X

[46] "Sysml faq: What is sysml?, why use sysml?, who created sysml?" http://sysmlforum.com/sysml-faq/, (Accessed on 12/11/2017).

[47] ISO, "Space systems - Design qualification and acceptance tests of small spacecrafts and units," International Organization for Standardization, Geneva, CH, Standard, Jul. 2017.

XIV. APPENDIX A

Tables XIV, XIV, XIV and XIV show the mission success criteria, functional requirements, non-functional (operational) requirements and constraints, respcectively.

TABLE XXIV

MISSION SUCCESS CRITERIA

Req. ID	**Definition**	Min	Full
M-0-001	S/C shall successfully launch, deploy, detumble and initialize operations (LEOP and commissioning) in LEO	✓	
M-0-002	Mission control shall identify S/C, generate TLE and estimate its initial state upon deployment from P-POD with max $\pm$ 30% deviation allowed to nominal orbit	✓	
M-0-003	Shall observe Case 2 water area in Norwegian coast of $\leq 70 \times 70$ km^2 at view angle $\leq 70^\circ$ with respect to Nadir	✓	
M-0-004	Should observe Case 2 water area in Norwegian coast of $\leq 200 \times 200$ km^2 at view angle $\leq 20^\circ$ with respect to Nadir		✓
M-0-005	Shall pass target at least 1 pass per day	✓	
M-0-006	Should pass target at least 3 passes per day in Spring time		✓
M-0-007	Shall, under cloudless or cloud gap conditions, take at least 3 image of target area with ≤ 20 bands in VIS-NIR spectral range that contains a detectable water-leaving signature to be ground truthed	✓	
M-0-008	Should, under cloudless or cloud gap conditions, take at least 30 images of target area with ≤ 100 bands in VIS-NIR spectral range that contains detectable water-leaving signatures to be ground truthed		✓
M-0-009	S/C shall take images while pointing Nadir and achieve at least 10 % overlapping fields	✓	
M-0-010	S/C should perform slew maneuver along one axis at a constant rate with two actuation events of reaction wheels and take images with at least 80 % overlapping fields that will undergo super-resolution post-processing to get at least $\sqrt{3}$ better SNR and spatial resolution in average		✓
M-0-011	Shall downlink at least spatially compressed data in raw format	✓	
M-0-012	Shall enable flexible mission planning & scheduling and subsystem updates through uplinked data	✓	
M-0-013	3 onboard processed image and TT&C data shall be downlinked for direct interpretation	✓	
M-0-014	10 onboard processed images and TT&C data shall be downlinked for direct interpretation		✓
M-0-015	Shall communicate to ground and downlink house-keeping telemetry data for at least 1 pass per day	✓	
M-0-016	Should communicate to ground and downlink house-keeping telemetry data for each available pass per day		✓
M-0-017	Shall be operational for at least 6 months with daily mission updates during peak-season	✓	
M-0-018	Should be operational for at least 3 years with daily mission updates during peak-season		✓

TABLE XXV

MISSION FUNCTIONAL REQUIREMENTS

Req. ID	Definition
M-1-001	Shall achieve LEOP plus commissioning in less than 2 weeks with full mission operations support in less than 3 weeks
M-1-002	Detection and identification of scientific matter in mesoscale target area shall happen in at least in 1 out of 72 orbits in spring and summer season with less than 10 % false positive signatures
M-1-003	Target area shall be any area with mesoscale size of at least 70×70 km^2 along the coast of Norway that will include the point at Lat: 63.867608 $^\circ$ and Lon: 8.663644 $^\circ$ and be imaged between 08:00 AM and 13:00 PM in spring and summer season
M-1-004	50 % of target area image shall be without brightness saturation due to sun-glare
M-1-005	S/C payload shall have spectral range of at least 400-800 nm (VIS-NIR) and spectral resolution of ≤ 10 nm
M-1-006	Images of target area with positive signatures shall have spatial resolution of $\Delta x \leq 100$ m, ≥ 20 spectral bands at ≤ 10 nm resolution, and mapping knowledge error of $\leq \pm 10$ m
M-1-007	Remote sensing images with positive signatures shall have $\leq 100 \times 100$ m^2 spatial resolution, i.e. $\Delta x \leq 100$ and $\Delta y \leq 100$ m and GSD ≤ 100 m
M-1-008	Faintest detectable ToA signature in the range of 400-600 nm range shall be at SNR of 200:1 for algorithm detection
M-1-009	Angle between initial target area point and Nadir, e.g. view zenith angle or sensing axis-target angle, shall not exceed 70°
M-1-010	Shall enable automated on-board geometric (situational awareness) processing/calibration; radiometric processing/calibration; spectral compression; and spatial compression in the respective order
M-1-011	Shall fuse overlapping fields of view in order to enhance the image resolution by a factor of at least 3 and mean SNR of at least $\sqrt{3}$
M-1-012	Shall have on-board radiometric and geometric calibration resulting in $\leq 15\%$ radiometric uncertainty and ≤ 10 % geometric uncertainty
M-1-013	Target area shall be viewed with a total of 3 observable passes
M-1-014	Shall downlink at least 3 images per day and perform 3 full and nominal imaging operations per day when signatures are detectable
M-1-015	At least raw data with ancillary information, including radiometric and geometric calibration coefficients and geo-referencing parameters (Level 1a) shall be downlinked
M-1-016	At least spectrally and spatio-temporally compressed data that are geometrically plus radiometrically calibrated onboard (Level 2 & Level 4) shall be downlinked
M-1-017	S/C shall have absolute pointing knowledge of $36''/0.01^\circ$ (2 σ) and absolute pointing accuracy of $360''/0.1^\circ$ (2 σ)
M-1-018	S/C shall slew in 3-axis prior to image acquisition such that S/C points maximum $+60^\circ$ with respect to Nadir and in direction of orbit-track with settling time ≤ 1 min and drift error $\leq 0.01^\circ$
M-1-019	S/C shall slew in 3-axis in opposite direction of orbit-track with maximum slew rate of $1^\circ/s$ in image acquisition mode during $\leq$ 1 min and drift error $\leq 0.01^\circ$
M-1-020	Response time of downlinked image with positive signature to in-situ validation in target area shall be less than 2 hrs
M-1-021	Spectral band selection and data bases on radiometric, geometric and atmospheric models shall be uplinked in maximum 3 orbits prior to the observations are made
M-1-022	Shall be inserted in a SSO configuration at altitude of 450-600 km with allowance of $\pm$ 23% deviation from nominal inclination angle
M-1-023	Shall be launched at 9:00-11:00 am or 8:00-10:00 pm LTAN with allowance of $\pm$ 10% deviation from nominal RAAN angle
M-1-024	Eclipse time shall be no more than 39.67 % of orbit period
M-1-025	Shall uplink data on mission planning & task execution with data size at max. 50 Mb
M-1-026	Shall downlink Level 2 or Level 4 data with data size at max. 300 Mb
M-1-027	Should downlink data of $>$ 300 Mb size in 3 consecutive orbits
M-1-028	Downlink data rate shall be at least 0.8 Mb/s at frequency between 2.60 to 3.95 GHz (S-band) and conform with the national frequency usage requirements
M-1-029	S/C shall conform to the CubeSat Specifications (Section 2) of the CubeSat Design Specification (CDS) rev. 12
M-1-030	Launch window for S/C should be maximum 4 months prior to spring season, specifically before or in February 2020
M-1-031	Launch window for S/C shall be maximum 8 months prior to summer season, specifically before or in June 2020
M-1-032	S/C shall accommodate axial acceleration of 7.2 gs, lateral acceleration of 2.4 gs, fundamental axial frequency of 30 Hz and fundamental lateral frequency of 12 Hz

TABLE XXVI

MISSION NON-FUNCTIONAL REQUIREMENTS

ID	Definition
M-2-001	Shall nominally map nominal target area each day without any apriori task commands on target location from Ground by slewing along-track with respect to Nadir, i.e. along in-track-Nadir (2-axis) plane and not pointing towards a target
M-2-002	Target location coordinates shall be uploaded from Ground based on visual inspection, in-situ assets other satellite data (e.g. MODIS, MERIS, Sentinel-3) within 24 hrs
M-2-003	Should point to and perform image acquisition of target areas where there is highest probability of detection off the coast of Norway
M-2-004	Shall perform imaging when conditions are cloudless or with cloud gaps, have solar zenith angle of $\leq 75°$ and wind ground speeds of < 12 m/s
M-2-005	Corrections for atmospheric distortions, water particles, aerosols, turbidity, clouds shall be enabled by utilizing $750 - 800$ nm (NIR) bands
M-2-006	Shall achieve GSD ≤ 100 m through 3-axis controlled slew maneuver to achieve effective image resolution of ≤ 100 m through post-processing algorithms
M-2-007	S/C shall be able to uplink and downlink from/to at least 2 ground stations being in Trondheim, Norway, and Longyearbyen, Svalbard
M-2-008	Mission planning & scheduling and pointing maneuvers shall be updated on-board through uplinked data in the same pass with lead time of minimum 5 min to the observations are made
M-2-009	Image acquisition and onboard processing of dataset shall happen during 2 min
M-2-010	Mean contact time during uplink and downlink of one image shall be 4 min and 5 min, respectively, and happen during same pass as observations
M-2-011	Ground shall have at least 1 available operator each day from 7:00 AM to 4:00 PM (UTC+1)
M-2-012	Downlinked and ground processed data should be available to other robotic agents, these being UAVs, USVs and AUVs, with response time of maximum 30 min to investigate positive signature detection(s) in target area
M-2-013	A shared model shall be updated on a data and model server between S/C, UAV, USV and AUV and other EO satellites and linked to payload data, navigational data and task execution and planning
M-2-014	Level 2 data shall consist of geometrically and radiometrically calibrated and geo-referenced hyperspectral images with up to 100 spectral bands and ≤ 10 nm resolution that have Gaussian average for each band
M-2-015	Level 4 data shall consist of target location and at least radiometrically calibrated hyperspectral images with up to 20 spectral bands and ≤ 5 nm resolution that have Gaussian average for each band
M-2-016	Mission shall support off/on payload operations during off-demand and NTNU shall have full uplink authority of model & camera updates to payload
M-2-017	Shall use on-board databases of on apriori-known reference spectral bands to detect, atmospheric models and environmental parameters for calibration and compression and enable payload to operate in different high-resolution and medium-resolution modes
M-2-018	S/C shall communicate to ground and downlink house-keeping telemetry data of up to 100 kb for at least 1 pass per day
M-2-019	Onboard databases on atmospheric models, solar angle conditions, weather models, sea state, target coordinates and usable spectral bands shall all enable payload to operate in unique modes according to the database used (e.g. gain tuning, exposure time, binning operations, and spectral compression).
M-2-020	Finer-scale images at mm-level resolution for identical parts of target area given positive detection(s) shall be provided by either UAVs, USVs and AUVs or all
M-2-021	Sub-surface water samples and in-situ measurements from identical parts of target area given positive detection(s) shall be provided manually or by either USVs, AUVs and buoys or all to give ground truth
M-2-022	Should support UAV, USV and AUV field campaigns through path-planning corrections and updates on geo-referenced target area coordinates
M-2-023	Shall accommodate distribution of Level 2 and Level 4 data to a maximum of 15 users
M-2-024	Shall accommodate distribution of Level 0 and Level 1a data for operational and payload performance characterization purposes for up to 5 users
M-2-025	Lifetime of NTNU SmallSat mission shall be at least 6 months and S/C shall de-orbit within 25 years
M-2-026	Shall have capability of being in idle mode while not imaging, thus only harvesting solar power in this mode while not in eclipse

TABLE XXVII

MISSION CONSTRAINTS

ID	Definition
C-001	Must adhere to at least 6 months of from delivery to launcher to the launch itself
C-002	Must adhere to frequency regulations set by the respective government where operations take place and frequency allocation determined
C-003	Must adhere to policy on SSA for tracking of Space Debris in LEO, thus enable de-orbit upon end-of-life within < 25 years
C-004	Project budget shall be within ≤ 16 MNOK for two missions
C-005	NTNU will partner with a third-party to do systems design, integration and testing and potentially launch, hence authority on results and operations needs to be negotiated
C-006	Launch shall, from a programmatic point of view, be scheduled in Q4 2019 with second mission in Q3 2020
C-007	Payload development needs calibration, characterization and testing prior to integration on S/C bus
C-008	Mission is a case study for academic (PhDs and Professors) research initiatives hence needs to be rigorously developed in terms of achieving publishable results
C-009	First mission needs a team of at least 10 people under its development from Phase A to Phase E, where 5 people are fully committed
C-010	S/C will piggyback on a launcher, hence the desired orbit is not guaranteed
C-011	Cloudy conditions are expected in Norway, hence results may not be satisfactory in terms of hyperspectral imaging up in northern latitudes